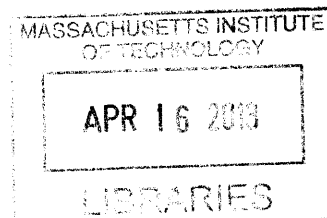


Bio-inspired Pressure Sensing for Active Yaw ARCHIVES
Control of Underwater Vehicles

by
Amy Gao



Submitted to the Department of Mechanical Engineering
in partial fulfillment of the requirements for the degree of

Master of Science in Mechanical Engineering

at the

MASSACHUSETTS INSTITUTE OF TECHNOLOGY

February 2013

© Massachusetts Institute of Technology 2013. All rights reserved.

Author
Department of Mechanical Engineering
December 5, 2012

Certified by
Michael S. Triantafyllou
Professor of Mechanical and Ocean Engineering
Thesis Supervisor

Accepted by
David E. Hardt, Professor of Mechanical Engineering
Chairman, Department Committee on Graduate Theses

11/10/10

Bio-inspired Pressure Sensing for Active Yaw Control of Underwater Vehicles

by

Amy Gao

Submitted to the Department of Mechanical Engineering
on December 5, 2012, in partial fulfillment of the
requirements for the degree of
Master of Science in Mechanical Engineering

Abstract

A towed underwater vehicle equipped with a bio-inspired artificial lateral line (ALL) was constructed and tested with the goal of active detection and correction of the vehicle's yaw angle. Preliminary experiments demonstrate that a low number of sensors are sufficient to enable the discrimination between different orientations, and that a basic proportional controller is capable of keeping the vehicle aligned with the direction of flow. We propose that a model based controller could be developed to improve system response. Toward this, we derive a vehicle model based on a first-order 3D Rankine Source Panel Method, which is shown to be competent in estimating the pressure field in the region of interest during motion at constant angles, and during execution of dynamic maneuvers. To solve the inverse problem of estimating the vehicle orientation given specific pressure measurements, an Unscented Kalman Filter is developed around the model. It is shown to provide a close estimation of the vehicle state using experimentally collected pressure measurements. This demonstrates that an artificial lateral line is a promising technology for dynamically mediating the angle of a body relative to the oncoming flow.

Thesis Supervisor: Michael S. Triantafyllou
Title: Professor of Mechanical and Ocean Engineering

Acknowledgments

First and foremost I would like to offer my sincerest gratitude to my advisor, Prof. Michael Triantafyllou, who has supported and guided me throughout my thesis while encouraging me to work my own way. With his patience and knowledge, and impressive ability to draw ideas together into elaborate and inspiring pictures, he has been a powerful source of both guidance and inspiration. I would also like to thank the number of other professors and research scientists at MIT who have helped me along the way - in particular, Prof. David Trumper for his help in resolving the electrical noise issues within my experiment, and Yuming Liu for his help with the formulation of my panel method simulation.

In my daily work I have been blessed with a friendly and cheerful group of fellow students and labmates. I would like to say a huge thank you especially to members of the Tow Tank Lab, Heather, Jeff, Audrey, James, Steph, and Jacob. The number of stimulating intellectual conversations we had both brightened my days and kept me thinking. Thank you also to Dr. Jason Dahl, who provided valuable advice in the brainstorming phase of this project and experimental design, and to our colleagues over in Singapore, who have offered helpful advice during our meetings.

Finally, I would like to express my love and indebtedness toward my family and my friends. To my dear parents, Tracy and Johnway Gao, thanks for bearing with me through all the happy times and all the hard times, and being a constant source of support and encouragement. I couldn't have done it without you guys! Thanks also for taking me tuna fishing. To my twin brother Allan - my lovable squishy, thanks for always being there for me, for advice, good stories, and good times. To Leah - thanks for always being there to listen and for helping me through many of the most difficult times of the last two years. And last but certainly not least, thanks to my boyfriend Richard, who has often had to bear the brunt of my frustrations against the world and overly long psets, code that won't compile, and experimental anomalies, but who has dealt with me with love and patience. I couldn't have done it without your love and support.

Contents

1	Introduction	17
1.1	Biological Inspiration: the Blind Cavefish	18
1.1.1	The Lateral Line: Structure and Function	19
1.1.2	Behaviors Aided by the Lateral Line	21
1.2	Relevant Work	22
1.2.1	Artificial Lateral Line Technology	22
1.2.2	Hydrodynamics of Lateral Line Stimuli	24
1.2.3	Lateral Line Feedback in Algorithm Development	24
1.3	Research Motivation	25
1.4	Chapter Preview	27
2	Hydrodynamic Background	29
2.1	Governing Equations	29
2.2	Modeling Pressure within the Fluid	30
2.3	Potential Flow	30
2.4	Superposition Principle	33
2.5	Application Within This Project	33
3	Testbed Construction and Experiments	35
3.1	Vehicle Design	35
3.2	Experimental Setup	37
3.3	Reduction of Noise in Experiments	38
3.4	Preliminary Experiments	39
3.5	Basic Controller Implementation	41
3.6	Dynamic Response	41
3.7	Physical Interpretation - Added Mass Effects	44
3.8	Concept of a Model Based Controller	46

4	Panel Method Forward Modeling	47
4.1	Comparison of Numerical Methods	47
4.2	3D Rankine Source Panel Method	49
4.2.1	Boundary value problem	50
4.2.2	Vehicle model	51
4.2.3	Integration over source panels	52
4.2.4	Far-field approximation	55
4.2.5	Reduction to linear problem and solution	55
4.3	Simulated Results	56
4.3.1	Model verification	56
4.3.2	Static pressure simulations	57
4.3.3	Dynamic pressure simulations	60
4.3.4	Dynamic pressure verification	64
5	Kalman Filter Inverse Modeling	65
5.1	The Kalman Filter	65
5.2	Applying the UKF to Estimate Yaw Angle	67
5.3	Results from UKF Implementation	70
6	Summary and Conclusions	73
7	Recommendations for future work	75
7.1	Optimization of the panel method	75
7.2	Physics-based learning model	76
7.3	Development of real-time control system	76
A	Additional Dynamic Pressure Simulations	77
B	Results from Various UKF Parameter Settings	83

List of Figures

1-1	Fish swimming in the ocean and dolphins breaching the water demonstrate the strength and versatility of marine animals (source: National Geographic).	17
1-2	Left: An underwater cave in the Yucatan Peninsula, Mexico where blind cavefish reside (source: National Geographic). Right: Blind cavefish in their natural environment (source: OpenCage Photography).	18
1-3	A photograph of a blind cavefish, overlaid with the approximate location of the canal lateral line and neuromasts within it.	19
1-4	Diagram of flow stimuli sources and the the lateral line system, with enlarged views of the superficial and canal neuromasts [45].	20
1-5	A - Cephalic lateral line system, displaying both the canal and superficial subsystems. B - Diagram of a canal neuromast, highlighting the composing elements. C - Photograph of a canal neuromast, within the canal. (source: Lab of Fish & Shellfish Pathology, Pukyong National University)	21
1-6	A sketch shows some capabilities enabled by the lateral line.	22
1-7	Left: the hydrocapped biomimetic superficial neuromasts manufactured by McConney et. al. [31]. Right: the SU-8 pillar superficial neuromast constructed by Kottapalli et. al. [28].	23
1-8	Left: the LCP and carbon black sensors constructed by Yaul [48]. Center and Right: Kottapalli et. al's LCP piezoresistive pressure sensors [28].	23
1-9	An artist's rendition of a submarine equipped with an artificial lateral line, exhibiting its ability to detect a school of fish swimming by (source: Chang Liu, University of Illinois).	26
2-1	Nomenclature used to define the potential flow problem (adapted from Low Speed Aerodynamics [27]).	31

3-1	A computer-generated rendering of the vehicle constructed for experiments.	36
3-2	Analytical solution for pressure field surrounding a Rankine body in steady uniform oncoming flow. The contours are equal-pressure lines (pressure marked in psi).	36
3-3	Frontal view and top view of nosecone, depicting the outlines of the channels cut to bridge the pressure ports and the pressure sensors. All measurements are in inches.	37
3-4	The towing tank facility in which the experiments were conducted. . .	38
3-5	A diagram of the experimental setup.	39
3-6	Summary of 33 constant yaw angle experiments, showing a roughly linear relationship between change in angle and the pressure measured at each port. Error bars show the standard deviation in each experiment set.	40
3-7	A proportional gain applied to the differential pressure is shown to predict the angle of the vehicle with high accuracy.	42
3-8	A Braitenberg controller aligns the vehicle with the flow following three large perturbations, which can be seen as variations of the dotted line, the actual angular position. The blue line represents the averaged differential pressure, which the proportional gain is applied to.	42
3-9	When a higher gain is applied, it can be seen that the controller overshoots zero degrees as it tries to correct the angle following a perturbation. The angle experiences decaying oscillations as it settles to zero degrees, but is still stable.	43
3-10	For an even higher gain, the system is critically stable. The angle never stabilizes to the desired zero degrees.	43
3-11	The NMP-like response seen in the sensor output when the vehicle turns. This results in initial angle correction in the wrong direction with the P controller, which is a cause of delayed response and possible instability.	44
3-12	The two differential pressures measured over a fast turn from 0 to 16 degrees and back to 0 degrees. The dotted line represents the motion profile.	44
3-13	The two differential pressures measured over a slow turn from 0 to 16 degrees and back to 0 degrees. The dotted line represents the motion profile.	45

4-1	Diagram of the discretized vehicle. The circular vehicle cross-sections are highlighted, and each point represents a corner point. The panels can be visualized as the space between any four points.	51
4-2	Diagram of the panel-centered frame of reference fixed to a quadrilateral constant-strength source element. The corners reflect the transformed coordinates of the corners (note that $z=0$), and P represents a point of interest. (adapted from Low Speed Aerodynamics, [27].	53
4-3	Left: The velocity potential calculated and plotted over the surface of a 400 panel sphere. Right: comparison between the analytical solution of velocity over the surface of the sphere and that calculated by the panel method.	57
4-4	Comparison between the surface pressure simulated using the source panel method and the doublet panel method, compared with experimentally measured pressures.	58
4-5	Comparison between the surface pressure simulated using the source panel method and the doublet panel method, compared with experimentally measured pressures.	59
4-6	The pressure field over the surface of the vehicle as it turns from 0 to 20 degrees, with the profile of the turn shown in the lower left hand plot. The diagonal lines in the background show the direction of the oncoming flow.	61
4-7	Pressure plotted against time and space (panel of the vehicle) for a) static pressure only (no turning), b) a constant velocity turn, c) a slowly accelerating turn, and d) a faster turn.	62
4-8	Pressure plotted against time and space for the fast turn. a) pressure outline for both sides of the vehicle during the turn. b) dynamic pressure outline for both sides of the vehicle during the turn. c) dynamic pressure measured at only the left sensors. d) dynamic pressure measure at only the right sensors.	63
4-9	Simulated (green) and experimentally measured (blue) pressure observed at 4 pressure sensors during a turn from 0 to 16 degrees and back to 0 degrees. Pressure (Pa) is plotted against time (s). The blue arrow represents the direction of oncoming flow.	64

5-1	A diagram illustrating the principle of the unscented transformation. Instead of propagating a single state estimate through a linearized function, a set of sigma points are propagated through the exact nonlinear function.	67
5-2	A comparison between the actual angle the vehicle is at during an experiment, the estimated angle as produced by the Unscented Kalman Filter, and the estimated angle as produced by the proportional estimator.	71
5-3	A comparison between the actual angle the vehicle is at during an experiment, the estimated angle as produced by the Unscented Kalman Filter, and the estimated angle as produced by the proportional estimator.	71
A-1	Simulated (cyan) and experimentally measured (blue) pressure observed at 4 pressure sensors during a turn from 0 to 16 degrees and back to 0 degrees, with maximum acceleration of 13 deg/s^2 . Pressure (Pa) is plotted against time (s). The blue arrow represents the direction of oncoming flow.	78
A-2	Simulated (cyan) and experimentally measured (blue) pressure observed at 4 pressure sensors during a turn from 0 to 16 degrees and back to 0 degrees, with maximum acceleration of 46 deg/s^2 . Pressure (Pa) is plotted against time (s). The blue arrow represents the direction of oncoming flow.	79
A-3	Simulated (cyan) and experimentally measured (blue) pressure observed at 4 pressure sensors during a turn from 0 to 16 degrees and back to 0 degrees, with maximum acceleration of 65 deg/s^2 . Pressure (Pa) is plotted against time (s). The blue arrow represents the direction of oncoming flow.	80
A-4	Simulated (cyan) and experimentally measured (blue) pressure observed at 4 pressure sensors during a turn from 0 to 16 degrees and back to 0 degrees, with maximum acceleration of 100 deg/s^2 . Pressure (Pa) is plotted against time (s). The blue arrow represents the direction of oncoming flow.	81
B-1	Setting the measurement noise covariance to 10x the actual measurement noise reduces estimate oscillation, but increases the time delay, as shown in this simulation.	84

B-2	Setting the process noise covariance of yaw rate to 1/10th the noise covariance in yaw angle is shown to cause undershoot behavior which follows that in the measurement. This indicates some relationship between allowable unmodeled state change and estimated process noise.	84
B-3	UKF angle estimation produced by a simulated system with 4 sensors.	85
B-4	UKF angle estimation produced by a simulated system with 8 sensors.	85
B-5	UKF angle estimation produced by a simulated system with 18 sensors.	85
B-6	An experimental profile was provided to a simulated system capable of outputting model-accurate pressure measurements. The result demonstrates the dependence of convergence rate on the estimated measurement noise covariance (here, $R=70$).	86
B-7	Simulation with an estimated measurement noise covariance of $R=20$.	86
B-8	Simulation with an estimated measurement noise covariance of $R=3$. This case demonstrates the accuracy of the UKF state estimate when the measurement noise in the system is negligible. However, for the cases applied to experimental data, the high measurement noise introduces more oscillation of the estimate.	87

List of Tables

4.1 Comparison between FDM and panel methods.	48
---	----

Chapter 1

Introduction



Figure 1-1: Fish swimming in the ocean and dolphins breaching the water demonstrate the strength and versatility of marine animals (source: National Geographic).

Over millions of years, the bodies and brains of fish have evolved in many ways to achieve the objectives which render them capable of survival in the diverse and hostile environments of the oceans, rivers and seas. Extensive study and research have shone light on the incredible grace with which fish are able to maneuver, using their both sensitive and streamlined bodies to exploit the fluid mechanics of the water around them in a way that ocean engineers dream of emulating. A few of the most difficult objectives, which engineers and roboticists have striven to achieve for underwater vehicles and robotic fish in recent years, include station keeping under large perturbations, rapid maneuvering, power-efficient endurance swimming, and trajectory planning and tracking [7]. These challenges must be addressed through careful consideration and implementation of sensory capabilities, actuation, and control and planning mechanisms.

While research in actuation has yielded many underwater vehicles that are capable of high speeds and/or fast turns [1, 8, 19, 25], the successful application of these technologies will require faster and more precise underwater sensory systems. Without

high resolution sensors capable of fast data output, high performance in the obstacle-filled and unpredictable oceanic and littoral environments would be near impossible. In recognition of this need, we draw inspiration from nature to develop a new sensing technology based on a fish organ, the lateral line. As sensitive as a human's hearing system and directly integrated with the nervous system, it provides powerful local sensing which equips fish with the reflex-like qualities required for many behaviours, such as escape from predation and schooling. Despite the advantages that it clearly offers marine animals, engineers have yet to develop a technology like this for application on underwater vehicles. Such a technology could be transformative to the world of underwater robotics, by offering a fast and instinctive way to sense nearby flow structures and obstacles - a sense of touch at a distance. For the realization of such a sensor, much work remains to be done in understanding the nature of the flow in various scenarios, relating these hydrodynamic insights to theoretical pressure measurements, and developing control systems which are capable of utilizing the new knowledge.

Our work here focuses on one scenario and demonstrates the potential of an artificial lateral line within its capacity. In implementing the technology, we study the flow around a basic underwater vehicle, develop simulations which use that understanding to generate expected pressure measurements, and conclude with the development of a control system which uses artificial lateral line feedback to improve performance in the scenario.

1.1 Biological Inspiration: the Blind Cavefish



Figure 1-2: Left: An underwater cave in the Yucatan Peninsula, Mexico where blind cavefish reside (source: National Geographic). Right: Blind cavefish in their natural environment (source: OpenCage Photography).

The Mexican Blind Cavefish, *Astyanax mexicanus*, lives in the deep and beautiful underwater caves of Central America (Fig. 1-2), and it is famous for its lack of eyes. Given the mazelike stalagmite and stalagmite formations in the caves, researchers have been drawn to study them, asking the question of "how do these fish survive without eyes?" They found that in the absence of vision, the fish were forced to rely more heavily on their other senses, and as a result, those senses exhibited enhanced sensitivity. In particular, the fish were clearly able to sense the presence of nearby objects by detecting the change in flow surrounding their bodies, using an organ known as the *lateral line*.

1.1.1 The Lateral Line: Structure and Function

While the blind cavefish best demonstrates the aptitude of the lateral line, all fish possess this sensor in addition to their visual, olfactory, acoustic and tactile sensors. The lateral line consists of tens or even hundreds of hair cell sensors called neuromasts distributed over the body of the fish, and can be divided into two subsystems: the *superficial lateral line system* and the *canal lateral line system*. The superficial lateral line consists of neuromasts located on the surface of the skin, and detects the velocity of the flow. The canal lateral line system consists of neuromasts within subdermal canals (Fig. 1-3).

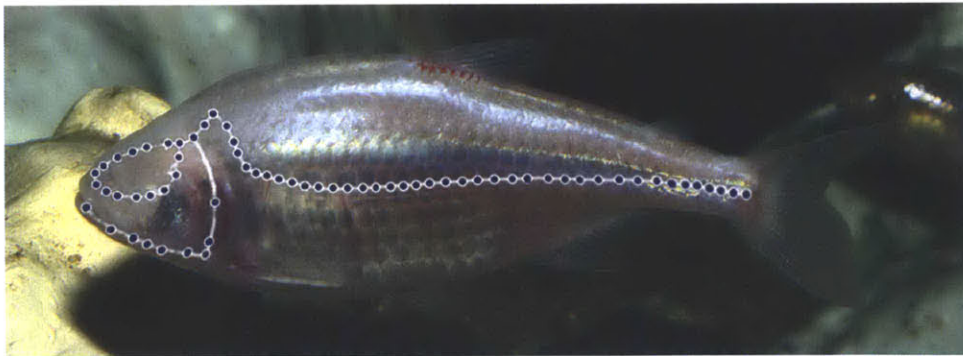


Figure 1-3: A photograph of a blind cavefish, overlaid with the approximate location of the canal lateral line and neuromasts within it.

Each neuromast consists of hair cells which are enclosed by a flexible, jellylike cupula, and acts as a mechanoreceptive organ which allows for the sensation of any movement [14]. While the neuromast is the functional unit of both subsystems, the morphology of the neuromast central to each is very different, in both size and shape (Fig. 1-4). This is largely due to function. The hundreds of superficial neuromasts on the fish surface interact directly with the flow, and are responsible for deflecting

as a result of small velocity changes. As a result, they are elongated and act as low pass filters to primarily to detect steady flow.

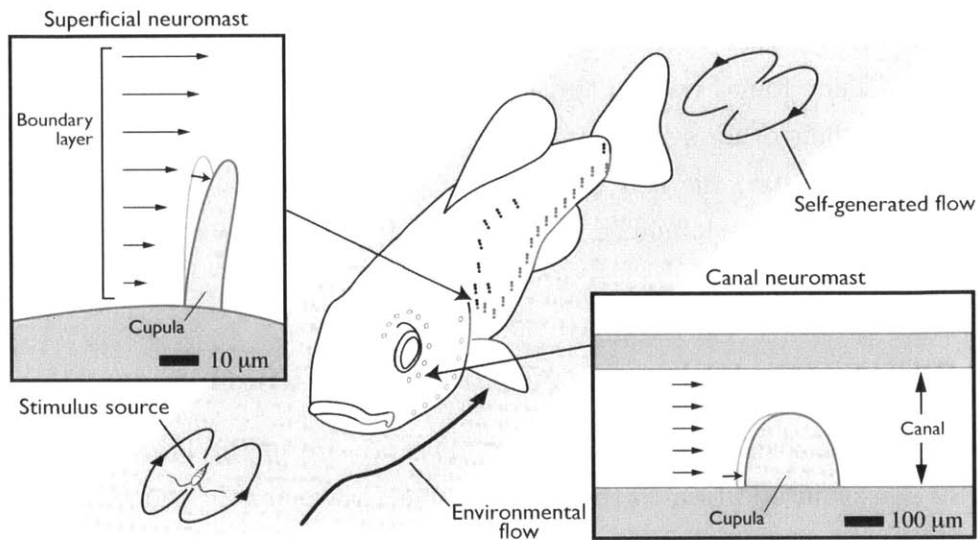


Figure 1-4: Diagram of flow stimuli sources and the the lateral line system, with enlarged views of the superficial and canal neuromasts [45].

In contrast to this, the neuromasts of the canal subsystem are fewer, larger and flatter. Each neuromast is enclosed within a canal, where there typically exists one neuromast between each set of regularly spaced pores. As water flows across the surface of the fish, pressure gradients are induced between the pores, which these canal neuromasts respond to [13]. As such, they act to detect changes in pressure. These pressure changes result from flow induced by variation of the current, movement of the body, the convergence of an object, or wake structures left by other animals [46].

In contrast to the superficial neuromasts, the canal neuromasts are not subject to the boundary layer of the body. As a result, while the fluid inertia within the canals still causes the system to act as a low pass filter, the neuromasts are less affected by the fluid velocity, allowing the system to be sensitive to a range of different stimuli.

In addition, it has been shown that the canals act to tune to specific frequencies of perturbations [41]. Widened canals are most sensitive to lower frequencies (under 60 Hz), such as those produced by movements of crustacean prey. While they tend to be more sensitive, they also respond more slowly due to the increased fluid inertia within the canals [14].

The canal lateral line system can be further divided into two canals - the trunk canal and the cephalic canal. The trunk canal typically consists of one linear canal which runs laterally down each side of the fish body, while the cephalic canal is more

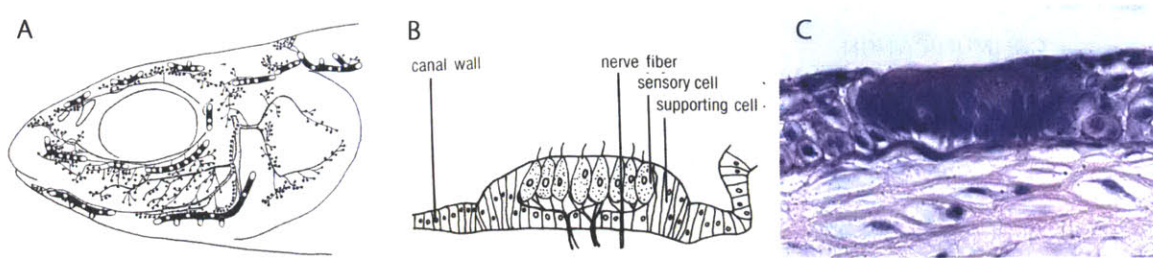


Figure 1-5: A - Cephalic lateral line system, displaying both the canal and superficial subsystems. B - Diagram of a canal neuromast, highlighting the composing elements. C - Photograph of a canal neuromast, within the canal. (source: Lab of Fish & Shellfish Pathology, Pukyong National University)

complex and forms a three-dimensional pattern around the head (Fig. 1-5), which varies between different species of fish. This allows for specialization of the cephalic lateral line to various tasks, such as mating and prey detection [40, 41].

1.1.2 Behaviors Aided by the Lateral Line

The lateral line has been shown to be fundamental to many fish behaviors, including object detection [11], the localization of moving prey and predators [11, 22, 41], and environmental mapping [5]. Although these applications are aided by other senses such as vision and smell, the lateral line is crucial to the speed and precision of behaviors such as the escape response [32]. In addition, in blind fish such as *Astyanax mexicanus*, the lateral line is solely responsible for navigation through complex environments, response to dangers and prey detection [35, 46].

However, while it is easiest to recognize the importance of the lateral line for fish which are blind or are most active at night, this sensor aids in many responses for which other sensors (such as vision) do not provide any feedback. These activities include schooling [38], rheotaxis [34], and analysis of surface waves [3].

Most commonly, to test the influence of the lateral line, behavior is observed before and after anesthetization of the lateral line. With this technique, Coombs et. al. show that the mottled sculpin uses its lateral line to detect the vibration of mechanical dipoles, which were meant to simulate live prey [10]. Schwalbe et. al. used this technique to demonstrate that the peacock cichlid uses its lateral line to detect prey in the dark, thus reducing the competition and danger of feeding during the day [41]. Baker anesthetizes the lateral line in Antarctic fish to determine the responsiveness of the superficial and canal subsystems to various stimuli [2].

In one sense, the lateral line on a fish allows it to generate a local *hydrodynamic*

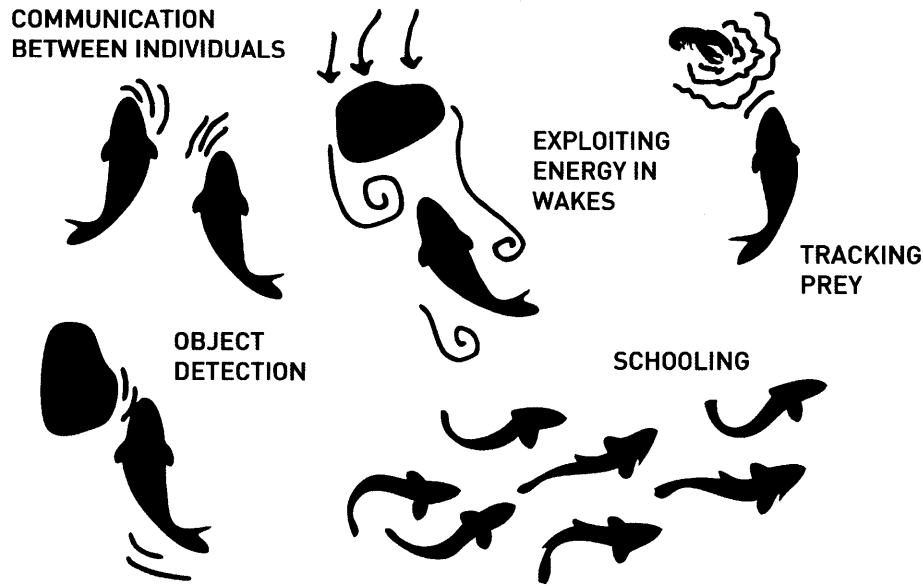


Figure 1-6: A sketch shows some capabilities enabled by the lateral line.

image of its surroundings. In order to understand how fish use this sensor to image its surroundings, it is important to study the nature of the flow field around the fish, and how this field changes as it is subject to different flows and perturbations. By developing a generalized theory surrounding this, it will then be possible to determine how the fish is able to detect the shape of the flow, and decode the patterns to sense the presence of objects, other fish, predators, and prey.

1.2 Relevant Work

1.2.1 Artificial Lateral Line Technology

Toward the creation of an artificial lateral line, several past studies have centered on the development of microelectromechanical systems (MEMS) technology for the creation of an artificial lateral line. The majority of these focus on developing pillar-like mechanical structures which mimic the superficial neuromasts of the lateral line [15, 28, 31, 47]. In these, a pillar is used to simulate the cupula of the neuromast, and various types of strain gauges are typically used to measure the deflection of the pillar as it is subjected to different cross-flows. In some, the mechanical pillar is additionally capped with a hydrogel or similar material to simulate the mechanical properties of biological neuromasts. This was shown to significantly decrease the lower threshold

limit of flow detection and expand the dynamic range of operation due to suppression of background noise [31, 39].

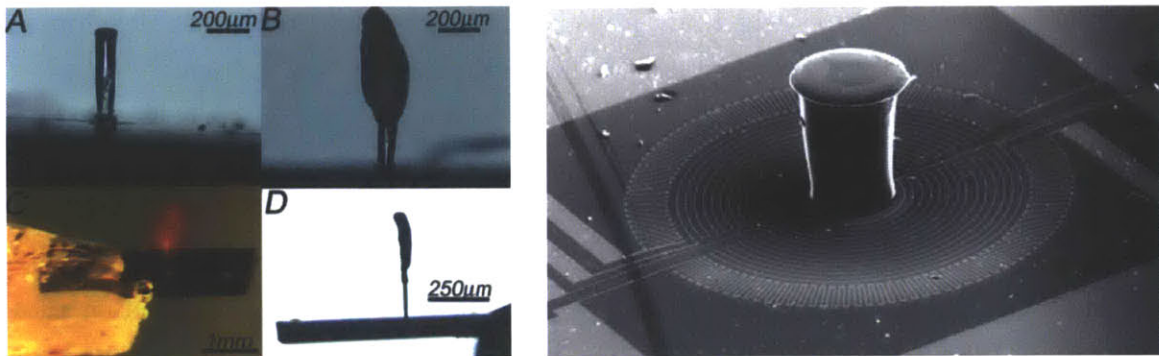


Figure 1-7: Left: the hydrocapped biomimetic superficial neuromasts manufactured by McConney et. al. [31]. Right: the SU-8 pillar superficial neuromast constructed by Kottapalli et. al. [28].

The canal neuromasts have the more general function of detecting pressure, which many commercialized sensors are already capable of doing. As a result of this, a fewer number of studies have aimed to construct sensors which mimic the canal neuromasts of fish. In the ones that do, the majority implement off-the-shelf pressure sensors, which they incorporate into arrays. Hsieh et. al. constructed a sensor array from a high efficiency and low cost piezoelectric material, Polyvinylidene Fluoride (PVDF), which generates an electric potential or electric field in response to applied stress [24]. Kottapalli et. al. developed a MEMS pressure sensor comprised of a liquid crystal polymer (LCP) membrane which encased thin film gold piezoresistors [28]. One study aimed to develop geometrically simplistic and low-cost flexible pressure sensors [48]. These consisted of patterns of conductive carbon black encased in LCP. By detecting the change in resistance of the carbon black as the the sensor deflected, the pressure surrounding the sensor could be deduced.

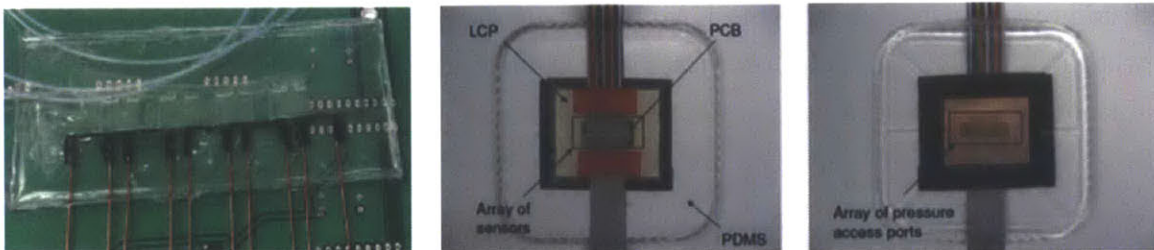


Figure 1-8: Left: the LCP and carbon black sensors constructed by Yaul [48]. Center and Right: Kottapalli et. al's LCP piezoresistive pressure sensors [28].

1.2.2 Hydrodynamics of Lateral Line Stimuli

Numerous studies have been performed to study the various stimuli to the lateral line, and the flow structures which are produced by them. It is crucial to develop a strong understanding of these effects in realizing the lateral line technology. While different flows and pressures may be detected by increasingly accurate and sensitive MEMS pressure sensor arrays, this information possesses very little value without a methodical way to interpret it. As such, many groups have studied the response of the lateral line to dynamic vibrations, nearby objects, and vortices.

Vibrations are characteristic of nearby prey, and many groups have studied the sensitivity of the lateral line to this stimulus in order to understand its structure and effective range. By far, most studies which are concerned with this use a mechanical dipole oscillating in the range of 50 Hz. to produce the vibrations [6, 9, 12]. These studies have isolated the detection of vibration to the canal lateral line system, and have found that the range of detection is typically about 1.5 times the body length [9].

Another stimuli that has been widely studied is the vortex. Vortices are generated in many scenarios, including in the wake behind a bluff body such as a cylinder, and in the wake of a swimming fish. Fish in the wild often swim in the wake behind objects to save energy (Karman gaiting), and it is thought that the lateral line may help them mediate their position while doing so [29]. Given this, mathematical theories have been formulated to explain how vortices stimulate the canal lateral line [17], and numerous experiments have been conducted to test the effect of vortices passing by real or artificial lateral line systems [16, 17, 42].

Studies have also been performed to study the role of the lateral line in detection of solid objects. Although it is a passive sensor, the lateral line is capable of detecting the presence of solid, unmoving objects as a fish swims by them. This is due to the flow which is induced by the motion of the fish, which is distorted when objects are present. As such, the lateral line plays an important role in obstacle detection and collision avoidance. Experiments have been performed to study the ability of fish to detect such objects [20, 33], and experiments have also been performed to test the ability of artificial lateral line systems to detect and identify passive objects [30].

1.2.3 Lateral Line Feedback in Algorithm Development

Some groups have attempted to develop algorithms for use with MEMS artificial lateral-line sensors. Pandya et. al. have studied multisensor processing algorithms for underwater dipole localization [37]. Using an artificial lateral line composed of hot-

wire flow sensors, they developed a minimum mean-squared error (MMSE) estimator in conjunction with hydrodynamic theory based on a general acoustic dipole model. The algorithm was shown to determine the location of a dipole source positioned about 1 cm away with less than 5% error.

Algorithms have also been developed which focus on the localization and characterization of vortices and objects [16,18,30]. The work completed by these researchers typically demonstrate that capability to localize a vortex or object to within 5-10% of its true location. Characterization is typically a harder problem, though Maertens has demonstrated the ability to use an ALL mounted on an underwater foil to localize and determine the approximate size of a cylinder that it passes [30].

No projects known to the author have resulted in the development of full control systems which utilize artificial lateral line technology. All of the work mentioned demonstrates the feasibility of the artificial lateral line, but also highlighted the complexity of the inherent hydrodynamics, which must be mathematically defined, for development of appropriate control systems.

1.3 Research Motivation

In light of the previous work accomplished upon this topic, the focus of this project lies not within developing a microelectromechanical systems (MEMS) pressure sensor array for use as an artificial lateral line or in creating new methods of simulating flow and pressure surrounding an underwater body, but rather in applying hydrodynamic theory in developing the control algorithms necessary for using an ALL effectively to navigate underwater.

The majority of AUVs today use sonar and vision for imaging and navigation. However, these sensing systems are limited by blind zones, dark and murky environments, and processing speed. For this reason, they are very powerful when used on large vehicles for the illumination of a global environment, but they face the shortcomings of being difficult and time-consuming to interpret, incapable of operating in all environments, and occasionally too slow to sense dangers in time. This, in turn, limits the environments and speeds at which AUVs may operate. In contrast, an artificial lateral line would be constructed from an array of pressure sensors which is small, lightweight, low-cost, and requires extremely low bandwidth and power. A vehicle equipped with an ALL would have the ability to sense its local environment quickly and with high precision, allowing for fast and reflexive responses to dangers or obstacles (Fig. 1-9).

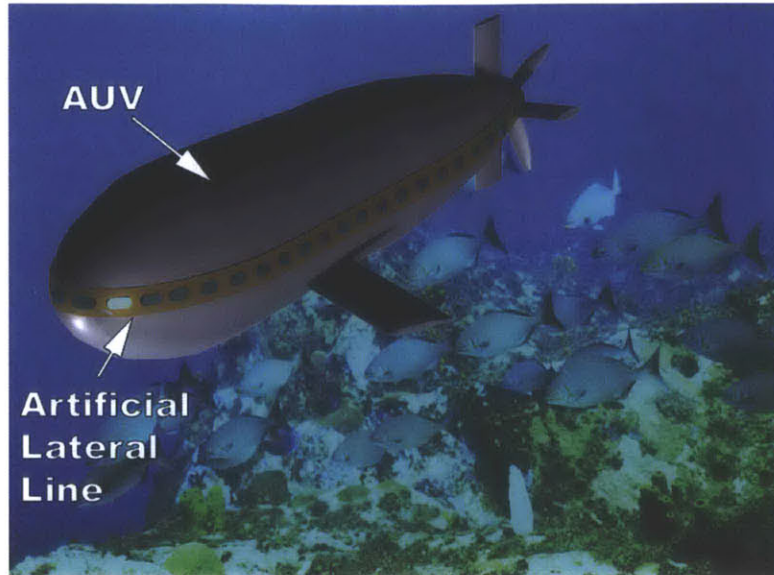


Figure 1-9: An artist's rendition of a submarine equipped with an artificial lateral line, exhibiting its ability to detect a school of fish swimming by (source: Chang Liu, University of Illinois).

In particular, an artificial lateral line system concentrated in the frontal region of an AUV could provide important information about incoming obstacles or changing flows. As previously described, the cephalic lateral line system on fish is a complex system of canals encircling the head. While the trunk lateral line only provides 2-dimensional information, the morphology of the cephalic system allows for 3-dimensional sensory capabilities which give rise to a diverse range of functions, including shoaling, prey detection and obstacle avoidance [44]. Given the importance of this system in spatial orientation and movement decisions, we focus solely on developing an artificial cephalic lateral line system in this project, and explore one of its functions - that of mediating the yaw angle of an underwater vehicle.

Mediating the yaw angle of an underwater vehicle is a useful function, as it allows for the vehicle to travel with the current instead of at an angle, reducing energy loss due to crossflows and minimizing control effort that would be used in fighting the strong munk moment that arises from traveling at angles. Furthermore, traveling with the current results in less drift and therefore less uncertainty in the vehicle position over time. Yaw angle detection can also serve as an additional feedback mechanism for state estimation, aiding in the task of vehicle localization.

The overarching goal of our work here is to develop a theoretical basis for understanding the surface pressure that results from different flows over the body of an underwater vehicle. With such an understanding, we can work toward the de-

velopment and implementation of control algorithms which are capable of using the feedback from an ALL effectively to detect and control a vehicle's orientation relative to a current. By showing that a small number of pressure sensors can be used to accurately detect the angle and used as feedback to return the vehicle to zero degrees relative to the flow, we provide a proof of concept that this technology can serve as a low-bandwidth sensor for a simple application. In addition, this project provides a framework for more complex applications, such as the control of an underwater vehicle in turbulent flow or in the wake of an object. In summary, it brings us one step closer to equipping modern AUV's with a mechanosensory underwater system which would be able to sense and utilize underwater flows and currents in a similar fashion to fish in nature.

1.4 Chapter Preview

In Chapter 2, the basic governing equations for this problem are presented, from a fluid dynamics perspective. Potential flow theory is introduced, and we comment on its qualities which make it an ideal modeling tool for this application. The concept of using elementary solutions to Laplace's equation as elements of a solid body is introduced, and the governing equations derived.

In Chapter 3, the experimental test setup and underwater vehicle are described. Several brief notes are included on the shape of the vehicle, and designing for reduction of mechanical and electrical noise. The experiments conducted are summarized and their most relevant results are presented. These include a set of static towing experiments, experiments conducted with a basic proportional controller implemented, and experiments conducted to test the dynamic response of the vehicle. Regarding the last, added mass effects are discussed, and their relevance to the problem is analyzed. Finally, the concept of a model based controller is introduced to address the issues brought up.

In Chapter 4, we develop the first component of a model-based controller: the model. Various computational fluid dynamics approaches are compared, and we motivate the choice of a panel method for modeling the vehicle. A 3D Rankine source panel method is chosen and developed. The boundary value problem is described, and we discuss how the panel method is used to solve the problem. Results from the final model are presented for simulations conducted at static yaw angles, and for dynamic maneuvers. For both, the simulated results are compared with previously collected experimental data, and there is good correlation.

In Chapter 5, we develop the second component of a model-based controller: the observer. Some background on state estimation and Kalman Filtering is first presented, followed by an introduction to the Unscented Kalman Filter. We describe how the UKF is used to predict the states of the vehicle, and discuss the key parameters. A few results from implementation of the UKF are presented, and are shown to produce much improved estimates, compared with the controller which operated on an estimate generated from comparisons against static pressure measurements.

Finally, in Chapters 6 and 7, the project is summarized and conclusions drawn, and a few recommendations for future work are provided.

Chapter 2

Hydrodynamic Background

This chapter will provide an overview of the general hydrodynamic theory which describes the flow around a 3D body.

2.1 Governing Equations

Within the fluid, we have conservation of mass:

$$\int \int \int_{V_m(t)} \left[\frac{\partial \rho}{\partial t} + \nabla \cdot (\rho \vec{v}) \right] dV = 0 \quad (2.1)$$

Which simplifies when we assume the fluid is incompressible:

$$\nabla \cdot \vec{v} = 0 \quad (2.2)$$

Conservation of momentum can be written:

$$\rho \frac{D\vec{v}}{Dt} = \rho \left(\frac{\partial \vec{v}}{\partial t} + \vec{v} \cdot \nabla \vec{v} \right) = \vec{F} + \nabla \cdot \tau \quad (2.3)$$

Where τ represents the stress tensor. This can be easily rewritten as Navier-Stokes equation:

$$\rho \left(\frac{\partial \vec{v}}{\partial t} + \vec{v} \cdot \nabla \vec{v} \right) = -\nabla p + \mu \nabla^2 \vec{v} + \vec{f} \quad (2.4)$$

In our case, viscosity is neglected, an assumption which will be justified at a later point. Setting viscosity to zero and rewriting the first term using the velocity poten-

tial, equation (2.4) becomes:

$$\rho \left(\frac{\partial \nabla \phi}{\partial t} + \vec{v} \cdot \nabla \vec{v} \right) = -\nabla p + \vec{f} \quad (2.5)$$

2.2 Modeling Pressure within the Fluid

The primary variable of interest is pressure, which is defined by Bernoulli's unsteady pressure law. This can be derived from equation (2.5) by expanding the second term on the left hand side and replacing the force vector \vec{f} with gravitational force. The cross product of the velocity and vorticity is:

$$\vec{v} \times \vec{\omega} = \vec{v} \times \nabla \times \vec{v} \quad (2.6)$$

$$= \vec{v} \cdot \nabla \vec{v} - \nabla \left(\frac{1}{2} \vec{v} \cdot \vec{v} \right) \quad (2.7)$$

For a potential flow, vorticity is zero, and so the left hand side of equation (2.6) is zero. Substituting the result into equation (2.5) and integrating out all the spacial derivatives, this yields Bernoulli's Unsteady Pressure law:

$$P = -\rho \left(\frac{\partial \phi}{\partial t} + \frac{1}{2} |\nabla \phi|^2 + gz \right) \quad (2.8)$$

Where ρ is the water density, ϕ is the velocity potential at the point of interest, g is the gravitational acceleration constant, and z is the current water depth. It is important to note that this is defined in the inertial frame of reference, and when we are concerned with the pressure at a material point (e.g. a point on the surface of a moving body), the equation must be rewritten to account for the material derivative:

$$P = -\rho \left(\frac{D\phi}{Dt} - v \cdot \nabla \phi + \frac{1}{2} |\nabla \phi|^2 + gz \right) \quad (2.9)$$

To solve, we must first analytically define ϕ .

2.3 Potential Flow

In hydrodynamics, potential flow describes the velocity field as the gradient of a scalar function.

$$\vec{v} = \nabla \phi \quad (2.10)$$

This allows for clear and analytical functions to be derived which represent various flows. Potential flow is limited to applications in which vorticity and turbulence are minimal, because the flow is assumed to be inviscid, incompressible and irrotational. As a result, it is best applied in high Reynolds number regimes, but when applied properly is capable of estimating the flow around complex geometries with high accuracy. For simulation of complex geometries, the elementary solutions of the potential flow problem may be distributed in a manner that satisfies the appropriate boundary conditions.

The mathematical problem can be illustrated by Figure 2-1. Here, we have rep-

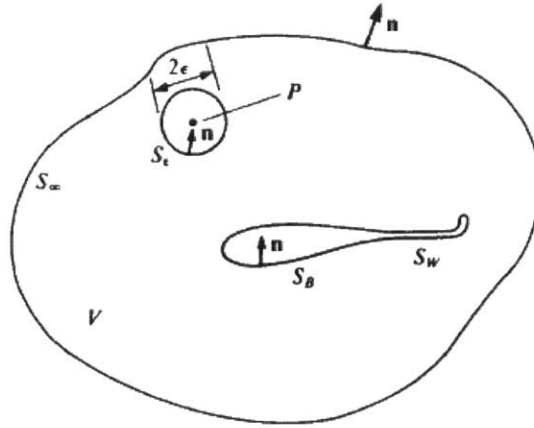


Figure 2-1: Nomenclature used to define the potential flow problem (adapted from Low Speed Aerodynamics [27]).

resented an arbitrary volume of fluid V in which we wish to solve for the flow characteristics. A body S_B within the fluid possesses a wake S_W . A designated point of interest is P , and the normal vector \vec{n} is defined to point outside of the region of interest. Where G is Green's function (the potential of a source) and ϕ represents the potential of the flow of interest (both scalar functions of position), the divergence theorem gives:

$$\int_S (G\nabla\phi - \phi\nabla G) \cdot \vec{n} dS = \int_V (G\nabla^2\phi - \phi\nabla^2 G) dV = 0 \quad (2.11)$$

In the case where P is outside of the fluid volume of interest, both G and ϕ satisfy Laplace's equation, so the right hand side of the equation goes to zero. To extract P from V , we enclose it in a small circle of radius ϵ . Rewriting equation 2.6, this yields:

$$\int_{S+\text{sphere } \epsilon} (G\nabla\phi - \phi\nabla G) \cdot \vec{n} dS \quad (2.12)$$

Substituting in the definition of Green's function, $G = 1/r$, and expanding:

$$- \int_{\text{sphere } \epsilon} \left(\frac{1}{r} \frac{\partial \phi}{\partial r} + \frac{\phi}{r^2} \right) dS + \int_S \left(\frac{1}{r} \nabla \phi - \phi \nabla \frac{1}{r} \right) \cdot \vec{n} dS = 0 \quad (2.13)$$

Integration around the surface of the sphere gives $\int_{\text{sphere } \epsilon} dS = 4\pi\epsilon^2$, and assuming $\partial\phi/\partial r \approx 0$ because ϕ is likely a well-behaved function that will not vary much in the tiny sphere, the first term becomes:

$$- \int_{\text{sphere } \epsilon} \left(\frac{1}{r} \frac{\partial \phi}{\partial r} + \frac{\phi}{r^2} \right) dS = - \int_{\text{sphere } \epsilon} \left(\frac{\phi}{r^2} \right) dS = -4\pi\phi(P) \quad (2.14)$$

Finally, we substitute this back into equation 2.8 for a formula that provides the velocity potential at any point P , given the values of ϕ and $\partial\phi/\partial n$ on the boundary S :

$$\phi(P) = \frac{1}{4\pi} \int_S \left(\frac{1}{r} \nabla \phi - \phi \nabla \frac{1}{r} \right) \cdot \vec{n} dS \quad (2.15)$$

As a result, the problem is now reduced to finding these values on the boundary. As previously stated, to solve for the flow surrounding a complex shape, elementary solutions are distributed in a manner that satisfies the appropriate boundary conditions. The elementary solutions most commonly used in this context are the doublet (μ) and source (σ), where a doublet embodies the difference in potential between the inside and outside of a boundary, and a source represents the difference between the normal derivative of the inside and outside potentials:

$$\mu = -(\phi - \phi_I) \quad (2.16)$$

$$\sigma = - \left(\frac{\partial \phi}{\partial n} - \frac{\partial \phi_I}{\partial n} \right) \quad (2.17)$$

The potential at point P can now be rewritten in terms of these elementary solutions:

$$\phi(P) = -\frac{1}{4\pi} \int_S \left[\sigma \left(\frac{1}{r} \right) - \mu \frac{\partial}{\partial n} \left(\frac{1}{r} \right) \right] dS + \phi_W + \phi_\infty(P) \quad (2.18)$$

ϕ_W denotes the potential of a wake, in the case that the user wishes to define it for increased accuracy, and $\phi_\infty(P)$ denotes a constant potential in the region, which may be added for specific scenarios such as moving reference frames. This is the general form for the potential at a point P within a volume of interest, provided a known distribution of sources and/or dipoles over the surface of any bodies present within

the volume.

2.4 Superposition Principle

Up to this point, it has been implied that the total potential at any point can be found by summing individual contributions, or integrating over a contributing surface. This principle of *superposition* can be proven through the following example. If:

$$v_{r1} = \frac{\partial\phi_1}{\partial r} \quad \text{and} \quad v_{r2} = \frac{\partial\phi_2}{\partial r} \quad (\text{by definition}) \quad (2.19)$$

$$\text{then} \quad v_{r1} + v_{r2} = \frac{\partial\phi_1}{\partial r} + \frac{\partial\phi_2}{\partial r} \quad (2.20)$$

provided the boundary conditions are linear, which is the case for rigid non-moving walls or infinite space. Equivalently, if we let $\phi = \phi_1 + \phi_2$,

$$v_r = \frac{\partial\phi}{\partial r} = \frac{\partial}{\partial r}(\phi_1 + \phi_2) = \frac{\partial\phi_1}{\partial r} + \frac{\partial\phi_2}{\partial r} \quad (2.21)$$

This linear property means that if the velocity potential is known for two different flows, then the sum of the two flows will also be a solution to Laplace's equation. This indicates that a complex flow can be formulated by summing any number of elementary solutions.

While this concept seems straightforward, it is this idea which makes potential flow theory so powerful, because it allows for the formulation of complex 3-dimensional flow problems as linear problems. This eliminates the need to solve the governing differential equations for each fluid element, which would be a lengthy and computationally taxing process. Therefore, if a flow problem can be modeled using potential theory, finding its solution becomes a far faster and more manageable process.

2.5 Application Within This Project

Within this project, the problem description involves a 3D body which moves through a fluid volume, translating and rotating over time. We aim to calculate the potential on the surface of the body, provided the state of the vehicle (position and velocity of each point). Given the potential, the surface velocity and surface pressure can then be obtained. To solve for these parameters, we require a discretization of the body geometry, definition of source and/or dipole locations and strengths over the body. Panel methods are a well-studied approach for this type of problem, and its

application within this context will be covered in Chapter 4.

Chapter 3

Testbed Construction and Experiments

A testbed was constructed to investigate the feasibility of using an artificial lateral line system for yaw angle feedback within a control system. The setup allows for testing to occur in a more controlled environment, where parameters such as flow speed and angle can be precisely dictated, and the dynamics of a vehicle with thrusters and control fins does not have to be considered. To address the goal of estimating and correcting a vehicle's angle of attack, sensors mounted on the experimental vehicle act as a simplistic replica of the fish's cranial lateral line system. This subsystem was chosen as the focus because its location imparts upon it exceptional sensitivity to pressure fluctuations resultant of changes in orientation.

3.1 Vehicle Design

The setup consists of a towed underwater vehicle (measuring 0.7 m long by 0.15 m diameter) with five off-the-shelf pressure sensors (Freescale MPXV7007) mounted at the head (Fig. 3-1). The MPXV7007 sensors are monolithic silicon piezoresistive transducers in a thermoplastic (PPS) surface mount package. They feature a range of -7 to 7 kPa and 5% maximum error over 0° to 85°C, and are internally amplified to output a signal between 0.5 and 4.5 V. The analog signals are read by an NI USB-6009 data acquisition unit, and processed using code written in LabVIEW (National Instruments, Austin, TX).

The shape of the vehicle was chosen such that the nosecone resembles a 3D Rankine body, for which an analytical solution to the flow disturbance within a steady uniform oncoming stream is readily available (Fig. 3-2). The pressure ports are chosen to be

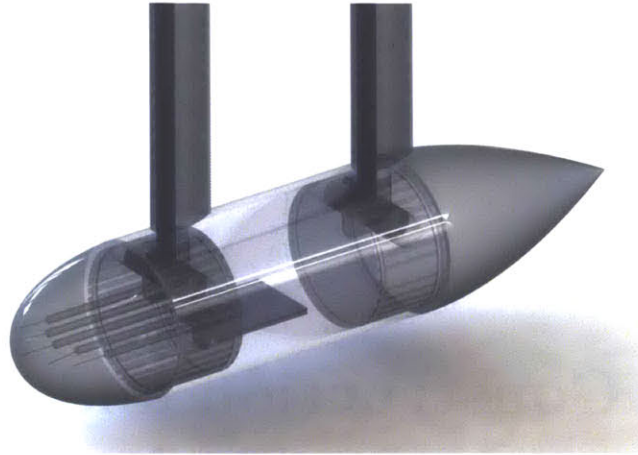


Figure 3-1: A computer-generated rendering of the vehicle constructed for experiments.

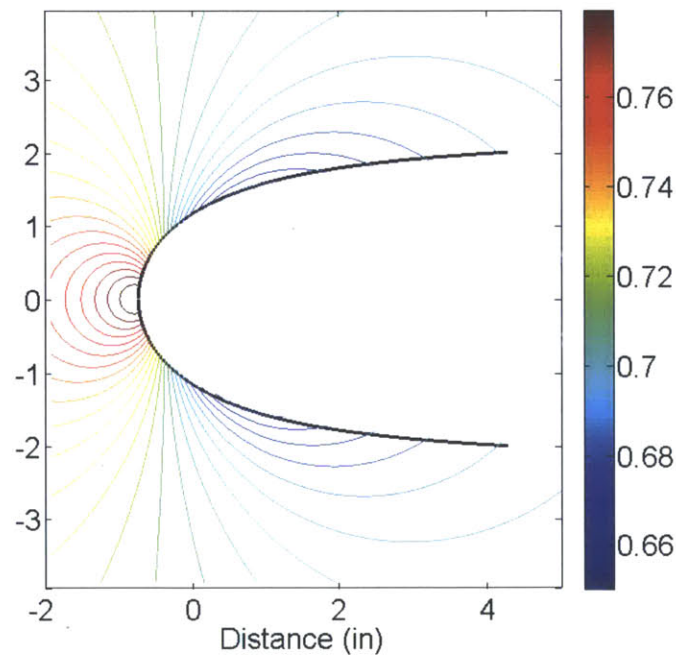


Figure 3-2: Analytical solution for pressure field surrounding a Rankine body in steady uniform oncoming flow. The contours are equal-pressure lines (pressure marked in psi).

laterally spaced 0.88 inches apart. Interior channels within the nosecone act to bridge the pressure ports to the sensors mounted within the body. In this way, the sensors are not directly exposed to water (MPXV7007 sensors are not compatible with water). In addition, this structure is easier to construct, because it eliminates the need to mount the sensors to the inside of the curved nosecone. Due to manufacturing constraints,

the channels were constructed to be wider near the inside and narrower at the surface. Calculations were performed to ensure that the narrow region was sufficiently long to prevent water from entering the wide channel. A drawing of the nosecone architecture is presented in Figure 3-3.

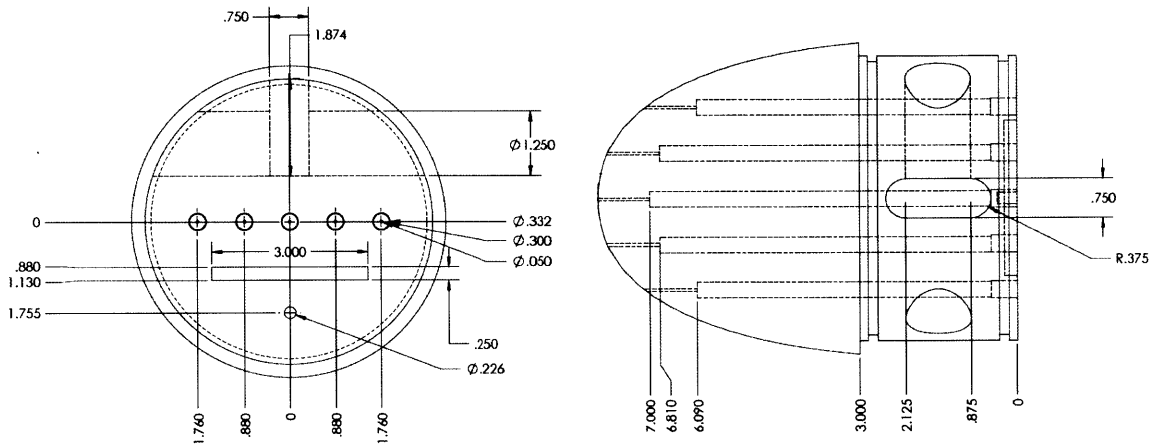


Figure 3-3: Frontal view and top view of nosecone, depicting the outlines of the channels cut to bridge the pressure ports and the pressure sensors. All measurements are in inches.

The tail section tapers to a point, streamlining the vehicle. This acts to reduce flow separation. While separation would likely not affect pressure measurements at the front of the vehicle, reducing separation acts to reduce oscillatory body forces which would result in greater mechanical vibration.

Both the nosecone and tail section were manufactured by CNC lathe from high density polyethylene (HDPE). The material provided a smooth finish when turned with a high speed steel (HSS) cutting tool. The main body, or pressure vessel, is constructed from a 0.25 inch thick acrylic tube, sealed at both ends with Buna-N o-rings inserted into rectangular grooves cut into the nosecone and tail section. Two steel shafts are allowed to rotate in bushings, and the supporting rods are directly threaded into them. The rotation allows for pitching maneuvers of the vehicle, which were unexplored within this project but could be a direction for future work.

3.2 Experimental Setup

The experiments were carried out in the MIT Towing Tank, a 33 m long pool that is approximately 2.6 m wide and 1.2 m deep (Fig. 3-4). The testbed is mounted to a carriage which is driven down the length of the tank by a simple drive system.



Figure 3-4: The towing tank facility in which the experiments were conducted.

To produce carriage motion, a Compumotor brushless DC servomotor drives a pulley system. The vehicle is mounted to the carriage via two steel rods, which are enclosed in streamlined aluminum tubing struts to minimize mechanical vibrations that would occur as the result of separation of the flow surrounding the rods. The carriage is towed at a fixed rate of 1 m/s for all experiments. A Copley STA2510 direct drive motor mounted to the carriage actuates the vehicle in yaw, to achieve or maintain various angles of attack. A position sensor within the motor allows for angular position feedback. A computer and other supporting hardware are also located on the carriage for vehicle control and data processing (Fig. 3-5). Pressure measurements were logged at a sampling rate of 1000 Hz.

3.3 Reduction of Noise in Experiments

Mechanical and electrical noise were nontrivial problems within this project. Several measures were taken to reduce each.

Mechanical noise was reduced by mounting the vehicle with two struts as opposed to one. Above the motor, a triangular strut mounts the assembly to the carriage, which further stabilizes the system. Within the vehicle, vibration of tubes can cause fluctuations in the measurements, and this was reduced by drilling channels directly into the nosecone, and connecting them to the sensors with extremely short tubes. Additionally, the vehicle was streamlined to reduce separation and vortex-induced vibrations (VIV), and the supporting rods were surrounded by streamlined tubing which rotated with the flow. This acted to reduce VIV from the supporting rods.

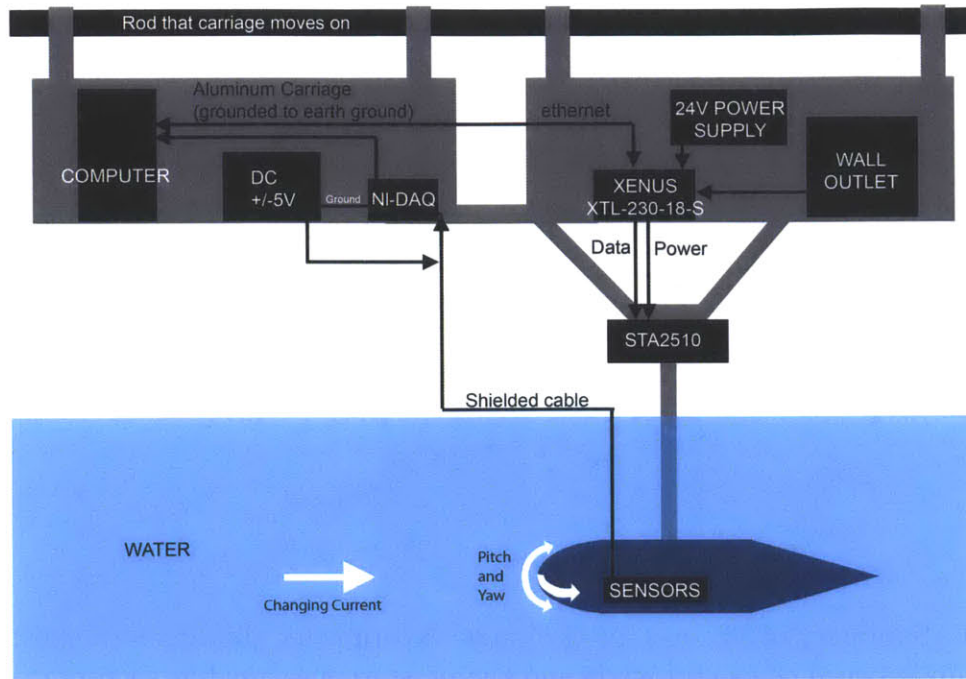


Figure 3-5: A diagram of the experimental setup.

Even with these precautions, some mechanical vibrations were still present. It could be possible to further reduce the vibrations by adding a third supporting rod to the assembly.

A large amount of electrical noise was present when the yawing motor was switched on. As the STA2510 is a powerful direct-drive motor, it is likely that it produces a large amount of electromagnetic interference. To reduce this, the motor drive was grounded to the metal carriage, and separate power supplies were used to power the sensors and the motor hardware. Shielded wires were used to transmit the sensor signals, and RC filters were installed between the cables and the DAQ to filter out high frequency noise. Furthermore, as the motor drive unit is powered through the wall outlet, there may be increased noise from the AC signal. To reduce this, an isolation transformer was placed between the wall outlet and units it supplied (motor drive, power supply).

3.4 Preliminary Experiments

The preliminary tests consisted of 33 constant yaw angle experiments - 3 tests each at two degree intervals between 0 and 20 degrees, in order to observe the relationship between yaw angle and pressure at the five sensor locations. These experiments

demonstrated the existence of a strong relationship between the angle of the vehicle and the pressure difference between the left and right sides of the vehicle (hereby referred to as the *differential pressure*). Averaged results from these experiments are presented in Figure 3-6. In this figure, the relationship between angle and pressure

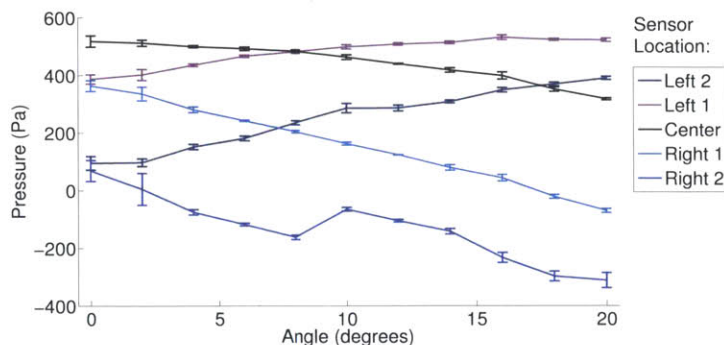


Figure 3-6: Summary of 33 constant yaw angle experiments, showing a roughly linear relationship between change in angle and the pressure measured at each port. Error bars show the standard deviation in each experiment set.

is roughly linear for all five ports. The data is very consistent within experiment sets, with an average standard deviation of 10.48 Pa for an average angle standard deviation of 0.13 degrees per experiment set (hard to align the vehicle at specific angles - there is some mechanical error which is recorded). The standard deviation for small angles is somewhat higher, possibly because the the relative angle deviation is higher, and for small angles the pressure is more sensitive to slight changes in angle. There is a small discrepancy in the data for the second sensor on the right. This is likely due to mechanical error. Due to the fast starts and stops of the carriage during experiments, some water may have entered the concerned channel. This would result in an increased pressure baseline, as the air in the channel cannot escape, and would be more compressed. Since the preliminary experiments were not intended to inform a control system, the experiments were not repeated.

The linear relationship between angle and pressure suggested that a Braitenberg type controller [4] might be able to regulate the angle of the vehicle by simply applying a proportional gain to the differential pressure observed. Braitenberg controllers were a concept introduced by Valentino Braitenberg in 1984 as a simple way to represent behavior based artificial intelligence. The premise is that a vehicle may possess a number of primitive sensors which are directly connected to effectors, such that a sensed signal immediately produces a particular motion. Depending on the architecture of the sensor-effector connections, the vehicle can be made to seem intelligent,

striving to achieve certain scenarios and avoid others. This type of controller appeared intuitively relevant to this problem, because it is easy to imagine that our vehicle might want to turn away from, or toward, higher pressure on one side. In the case of correcting an angle of attack, the vehicle would generally turn toward higher pressure, in order to minimize the pressure differential between its sides. Additional functions applied to the sensor outputs can create even more complex behaviors. For instance, a proportional controller applied to the pressure differential can create a smooth range of motion.

3.5 Basic Controller Implementation

A second set of experiments was conducted to test this concept. A proportional controller was developed in LabVIEW and implemented on the system, with the goal of returning the vehicle to zero degrees following any perturbations and maintaining that orientation. First, to determine an appropriate gain for the controller, a test was conducted in which the vehicle was sinusoidally yawed between -20 and +20 degrees, and the average pressure differential between the left and right sensors was recorded. The required gain was calculated by dividing the average differential pressure by the angle, and was found to be 16877 Pa/deg. By dividing the recorded differential pressure by this gain, it was found that the angle of attack could be recovered with high accuracy over the entire angle range (Fig. 3-7). The gain is likely to be highly dependent on oncoming flow velocity, so for different towing velocities, it would need to be adjusted. However, for small deviations, and for the altered apparent velocity at each port due to yawing and pitching, using a constant gain may be sufficient.

Implementing the Braitenberg controller with proportional gain, the vehicle was found to accomplish the goal of returning to zero degrees following perturbations (Fig. 3-8), but with a varying time lag. Furthermore, at higher gains, the system became unstable (Fig. 3-9, 3-10). This demonstrated the shortcomings of the Braitenberg controller, and suggested that a more complex, model-based controller would be required for improved system response.

3.6 Dynamic Response

To investigate the pressure fluctuation during dynamic maneuvers, a final set of experiments was conducted in which the vehicle was commanded to turn sharply from 0 to 20 degrees while being towed forward at 1 m/s. The differential pressure measured

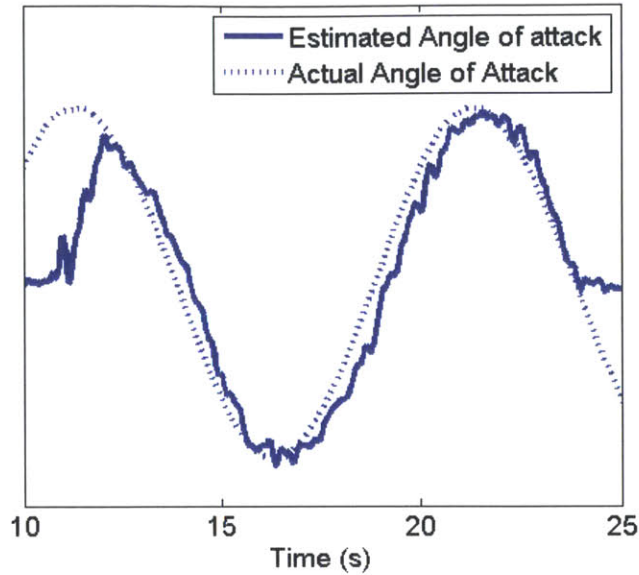


Figure 3-7: A proportional gain applied to the differential pressure is shown to predict the angle of the vehicle with high accuracy.

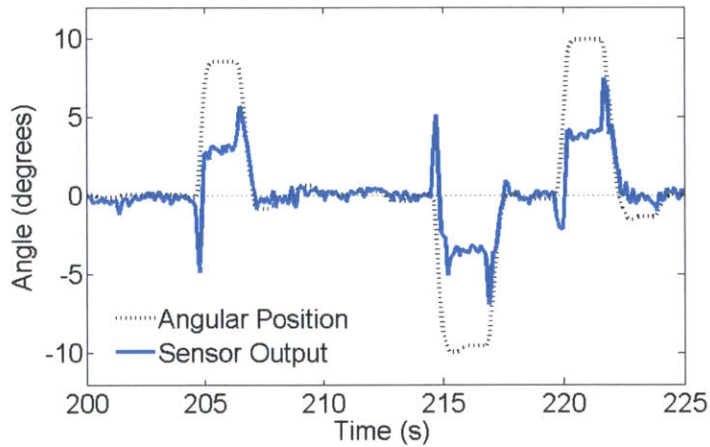


Figure 3-8: A Braitenberg controller aligns the vehicle with the flow following three large perturbations, which can be seen as variations of the dotted line, the actual angular position. The blue line represents the averaged differential pressure, which the proportional gain is applied to.

in one experiment is shown in Fig. 3-11. Here, we have focused in on the turning region so that the response can be clearly seen. These experiments revealed that when the vehicle turned from one static angle to another, the differential pressure response exhibited initial undershoot, a characteristic often seen in non-minimum phase (NMP) systems, which are generally challenging to control due to additional phase

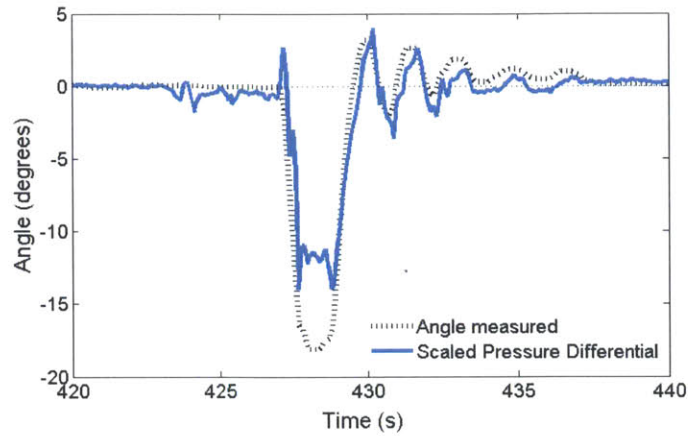


Figure 3-9: When a higher gain is applied, it can be seen that the controller overshoots zero degrees as it tries to correct the angle following a perturbation. The angle experiences decaying oscillations as it settles to zero degrees, but is still stable.

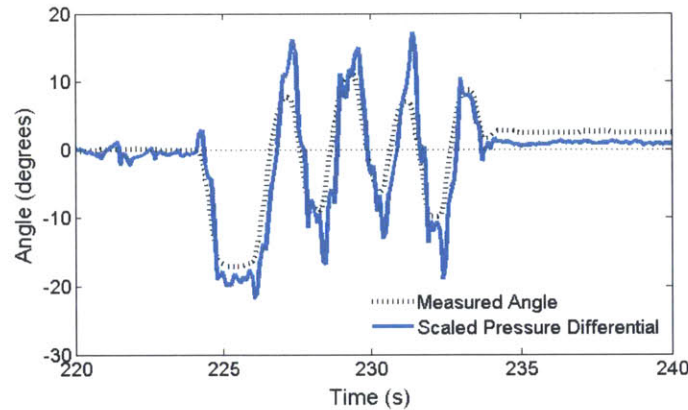


Figure 3-10: For an even higher gain, the system is critically stable. The angle never stabilizes to the desired zero degrees.

lag and limited achievable closed-loop bandwidth. The response observed causes time lag within the system, which can result in instability if it is too high.

Additional experiments were conducted to test the effect of different turning rates on the initial undershoot in sensor response. The response seen for two extreme cases, a fast turn and a slow turn, are shown in Figures 3-12 and 3-13, respectively.

The similarities between the response of an NMP system and the response of this system suggest that while a generic controller may be capable of maintaining the vehicle at zero degrees, a nonlinear model-based controller would be ideal, allowing for faster performance, robustness, and the ability to control turning to specific angles.

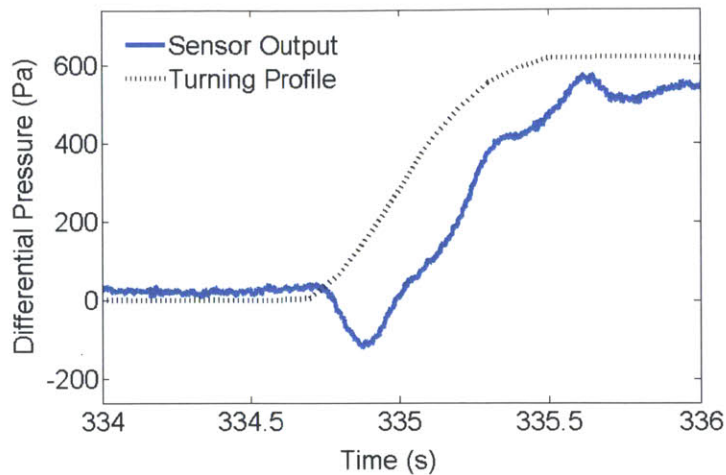


Figure 3-11: The NMP-like response seen in the sensor output when the vehicle turns. This results in initial angle correction in the wrong direction with the P controller, which is a cause of delayed response and possible instability.

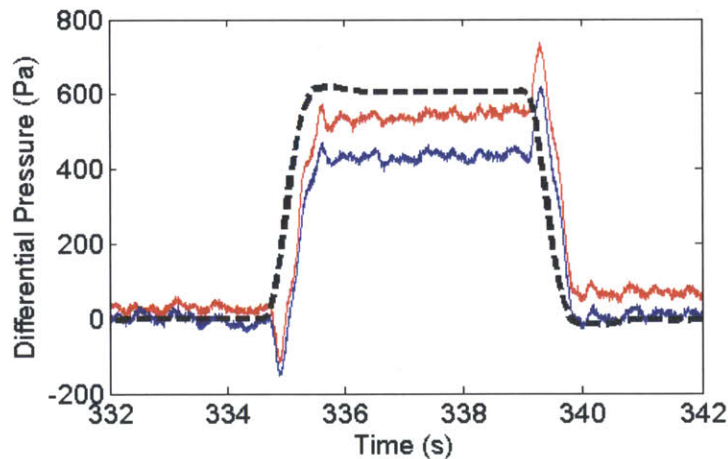


Figure 3-12: The two differential pressures measured over a fast turn from 0 to 16 degrees and back to 0 degrees. The dotted line represents the motion profile.

3.7 Physical Interpretation - Added Mass Effects

In mechanical systems, non-minimum phase behavior typically arises as a result of noncollocation, a physical separation of sensing and actuation. In this system, the separation between the yawing axis and the sensor port locations coupled with certain hydrodynamic effects likely cause this undesirable response. In particular, added mass, or virtual mass, accounts for high forces upon accelerating underwater. It can be thought of as the additional water mass that must be moved aside when a body pushes its way through water. This pushing results in higher pressures on the surfaces

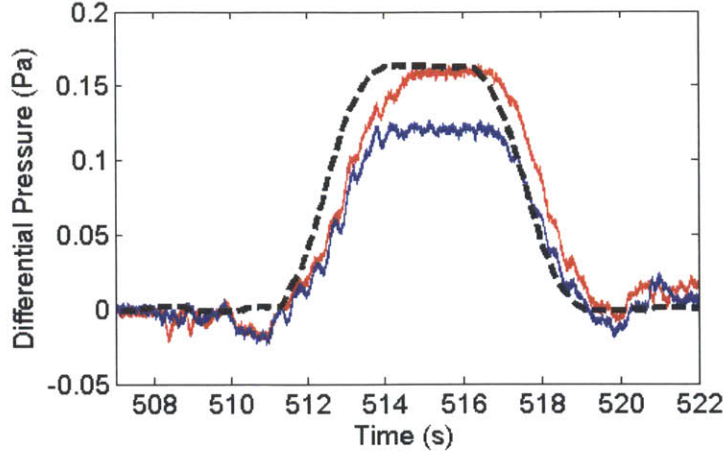


Figure 3-13: The two differential pressures measured over a slow turn from 0 to 16 degrees and back to 0 degrees. The dotted line represents the motion profile.

performing the pushing, and a suction effect on the opposite surfaces. While these effects are most often studied as body forces, the total force exerted on the body is a direct result of the pressure integrated over the surface of the body, where the pressure can be calculated from Bernoulli's unsteady pressure law. This relationship in the yawing direction, which produces a moment about the z axis, is:

$$M_z = \int \int_B - \left(-\rho \left(\frac{\partial \phi}{\partial t} + \frac{1}{2} |\nabla \phi|^2 \right) \cdot \vec{n} \right) \times \vec{r} dS \quad (3.1)$$

$$= -\dot{U}_i m_{6i} - \epsilon_{3kl} U_i \Omega_k m_{l+3,i} - \epsilon_{3kl} U_i U_k m_{li} \quad (3.2)$$

In the above formula, the term within the integral is the dynamic pressure from added mass effects, which is integrated over the body. ϕ is the velocity potential at points on the body, \vec{n} is the normal vector pointing out of the fluid, and \vec{r} is the vector from the rotation center to each point on the body. The second formula is the formula for the moment about the z axis, in index notation, given the geometrical added mass coefficients of the body. Typically, these coefficients are unknown for complex geometries and must be calculated through numerical methods or experiments.

Physically, one could visualize the origin of the non-minimum-phase-like response by imagining a body which suddenly yaws left in the presence of oncoming flow. Initially, at zero degrees, the pressure on each side is roughly equal. As it executes a sharp turn, the pressure rises on the side the body turns toward, as the water is pushed out of the way. Then, as the body reaches its final angle, the high pressure region settles near the stagnation point, on the opposite side of the body. As a result,

any sensors placed on the left side would experience a pressure spike followed by a drop to a lower steady state pressure, and sensors on the right side would experience a pressure drop followed by a rise to a higher steady state pressure.

Added mass effects exist only in the presence of acceleration, so the sensors will measure a pressure transient during any unsteady linear or rotational maneuvers. Given that noncollocation contributes to the response, and the size of the transient is a function of the acceleration at the point of interest, one can expect that the initial undershoot observed would be smaller closer to the point of rotation and larger away from it. However, underwater vehicles typically turn about a point close to the center of mass, so high added mass effects can be expected near the head.

It is important to point out that while linear acceleration and rotational acceleration both engender added mass effects, the initial undershoot is only observed for rotational maneuvers. For linear acceleration the pressure transient occurs in the same direction as the overall steady state pressure change. The implication of this is that this effect is much more dangerous for turning maneuvers, where it can result in instability if the closed-loop system is forced to turn too quickly without accurate state estimation.

3.8 Concept of a Model Based Controller

Previously, it was hypothesized that experiments could be conducted to generate a lookup table that would provide the relationship between the yaw angle of the vehicle and the pressures measured at the sensor ports. This lookup table could then be used to estimate the angle of the vehicle and inform a control system that could correct the angle. However, it was found that in the presence of dynamic maneuvers or external flows, added mass effects result in pressure transients that invalidate the static angle estimates. Even in the presence of a steady flow, the maneuvering of a feedback-controlled vehicle would induce added mass effects that would cause erroneous feedback and possible instability. This effect was previously seen in Figures 3-9 and 3-10, where high gains caused oscillatory responses in the angle of the vehicle. Therefore, where fast and stable response is desired, a more complex controller must be used, which is capable of predicting added mass effects and factoring them into the angle estimate. Since added mass is a function of the vehicle geometry and motion, a model must be created to predict its effect. The model can then be used as the basis for a controller which accurately estimates the vehicle state and corrects it.

Chapter 4

Panel Method Forward Modeling

A model of the system should be capable of outputting relevant pressures (the pressures at each of the five sensor ports), provided the system state over time. As previously mentioned, the primary purpose of this model is to serve to estimate the added mass effects during maneuvers, which are geometry and state dependent. The nonlinearities in the problem and the infinite-dimensionality of the water suggest that a computational fluid dynamics (CFD) approach would be necessary for accurate results.

4.1 Comparison of Numerical Methods

Several different types of CFD were investigated, including panel methods, finite difference methods (FDM) and finite element methods (FEM). For FDM and FEM, the entire fluid volume surrounding the vehicle must be discretized into cells, which must be refined in the regions where the flow is expected to change rapidly. Each cell has a set of boundary conditions, and the Navier-Stokes equation must be solved within each cell. As a result, a complex set of nonlinear equations is produced, and solving the system numerically can be very difficult and time-consuming. There are generally a large number of gridpoints, as they must span 3 dimensions, and the order of the system is $\mathcal{O}[N^6]$, where N is the number of elements in each dimension. The solution produced is generally very accurate, since these methods are complete Navier-Stokes solvers, meaning they take into account viscosity and compressibility effects.

In contrast, panel methods are a type of Boundary Element Method (BEM), where only body surfaces need to be discretized into a surface mesh to find a solution to the problem. The surfaces are modeled as panels with some distribution of singularities

Table 4.1: Comparison between FDM and panel methods.

	FDM	Panel Methods
Grid Generation	fluid domain	body surfaces
Unknowns	Node values	Panel singularities
Number of unknowns	N^3	N^2
Order of system	N^6	N^4
Equation in domain	Approx.	Exact
Boundary conditions	Approx.	Approx.

over each. This works on the intuition that the flow is already defined in the entirety of the fluid domain, with the exception of the disturbance caused by the presence of a body. Therefore, to solve the problem, only the nature and strength of the disturbance must be determined. By assuming that the body can be modeled by elementary solutions (singularities), which are only present on the body surface, we can solve for the entire flow by finding the strengths of the singularities on the body. Since the use of singularities as a model assumes potential flow, these methods generally do not take viscosity and compressibility effects into account.

Panel methods originated in 1952-1953, in studying the flow about nonlifting bodies of revolution. Since their introduction, many advanced panel codes have been developed, such as PAN AIR, VSAERO, and HISS, which are widely used in industry. More complex codes typically involve higher order panels, nonuniform distributions of singularities over each panel, and corrections that allow for computation of viscous and compressibility effects. Even with these elements, panel methods are often simpler to program and faster than finite difference and finite element methods. Since the only unknowns are the singularity strengths on the body surfaces, panel methods reduce the 3D problem to a 2D problem, drastically reducing the number of calculations. As a result, there are $\mathcal{O}[N^2]$ panels and the order of the system is $\mathcal{O}[N^4]$, N being the number of panels in one dimension.

Once these influence coefficients for the problem are found, it reduces to a linear problem, which can be solved relatively quickly. It should be noted that panel methods are only applicable to problems for which Green's function can be calculated, which are typically only cases where the flow field is linear and homogeneous. Therefore, the problem should be studied carefully to determine if using a panel method is the correct approach. To summarize, Table 4.1 compares FDM and panel methods.

A panel method was ultimately chosen to model this system for its flexibility,

speed, and simplicity. While a number of complex panel codes are commercially available, a method was written which would be specific to this application, based on the procedure outlined by Hess [21]. Due to the simplifying assumptions of incompressibility, inviscid flow, and irrotationality, the code can be vastly streamlined. This allows for faster computation time, which is a critical condition for real-time control.

4.2 3D Rankine Source Panel Method

For this application, the vehicle is modeled using a first-order 3D Rankine Source Panel Method, a well-studied method of simulating incompressible potential flow [21, 27]. This classification implies that each panel is modeled as a flat (first-order) construct with continuous source strength which is constant over the area of the panel at each instant in time. This panel discretization will be clarified further at a later time.

The assumptions made in this work are that the flow is incompressible, inviscid, irrotational, and can therefore be completely defined by a hydrodynamic potential ϕ . This is a highly accurate assumption because for the region of concern (the front of the vehicle) in oncoming flow, the pressure gradient is extremely favorable, indicating that the flow is likely to be fully attached. The Reynolds number is approximately 150,000, indicating that inertial effects are high in comparison to viscous effects. Within this regime, panel methods are generally very accurate because the inviscid assumption is close to true.

With the panel method, the potential at any point due to each panel is obtained by integrating over the panel, and the final potential at a point \vec{x} comes from summing the influences of each individual panel. The formulation of this method was described in greater detail in Chapter 2, where equation 2.18 was derived, giving the potential of a body consisting of sources and dipoles. Here, we simplify the formulation by using only sources, and assuming the effect of the wake is negligible in the region of concern. In integral form, the equation is thus rewritten:

$$\phi(\vec{x}, t) = \int_S \sigma(\vec{\xi}, t) G(\vec{x}, \vec{\xi}, t) dS \quad (4.1)$$

Where ϕ is the vehicle disturbance potential, σ represents the source strength of some point on the body surface S , $\vec{\xi}$ is the vector to that point on the body, and G is Green's Function (the velocity potential of a point source). Constant strength source

panels were selected over dipole panels for their ability to generate smoother results, and the lack of necessity for simulating vorticity.

4.2.1 Boundary value problem

The integral equation (4.1) may be regarded as an exact solution to the governing Navier-Stokes equations. The panel method attempts to solve for the values of the source strengths σ within this equation, such that the boundary conditions of the problem are satisfied. The specific solution of velocity or pressure is then calculated through a secondary set of equations.

The boundary value problem (BVP) is summarized as follows:

In the fluid, continuity yields:

$$\nabla^2\Phi = 0 \text{ and } \nabla^2\phi = 0 \quad (4.2)$$

Where Φ is the total fluid potential, given as:

$$\Phi(\vec{x}, t) = -Ux + \phi(\vec{x}, t) \quad (4.3)$$

U is the vehicle velocity in the inertially fixed x direction. On the surface of the body, the no-flux condition yields:

$$\frac{\partial\Phi}{\partial n}(\vec{x}, t) = \vec{v}(\vec{x}, t) \cdot \vec{n}(\vec{x}, t) \quad (4.4)$$

Where \vec{n} is the vector normal to the surface of the body at some point of interest, and \vec{v} is the water velocity at the same point. Finally, substituting the boundary conditions into the source panel method formulation (4.1) gives the final boundary value equation for the problem:

$$\int_S \sigma(\vec{\xi}, t) \frac{\partial G}{\partial n}(\vec{x}, \vec{\xi}, t) dS = \frac{\partial\phi}{\partial n}(\vec{x}, t) = Un_x(\vec{x}, t) - \vec{v}(\vec{x}, t) \cdot \vec{n}(\vec{x}, t) \quad (4.5)$$

This condition is solved numerically by discretizing the body geometry into 620 panels, assuming constant singularity strength over each panel, integrating over each to calculate its effect, and summing the contributions of each panel to solve for the hydrodynamic potential at a point of interest.

In defining the coordinates, we have chosen a reference frame which is fixed to the rotational center of the vehicle, but which maintains a fixed angular position with

reference to the inertial frame. This allows for a simplified transformation to panel-fixed coordinates, a step which is necessary in determining the influence of each panel through integration.

4.2.2 Vehicle model

Choice of how to discretize the vehicle into panels is very important, as the boundary condition is enforced only at the centroid of each panel. Therefore, a greater number of panels should be placed in regions of higher body curvature (where there is greater expected change of flow). The discretization of the vehicle, which is an axisymmetric body of revolution, is fairly simple to calculate. A grid of 32 points along the longitudinal (x) axis of the body was first constructed, allowing for more points in the front and back, where the curvature is higher. The points were spaced to allow for the known positions of the sensor ports to fall on panel centroids. Each circular cross-section was then divided into 20 equal segments. Corner points were then defined as the intersection of the $y - z$ planes along the discretized x axis, the surface of the vehicle, and the angular cross-section divisions, as shown in Figure 4-1. In this case, the panel collocation points (also known as control points) were defined as the average of the four corners (the centroid), following simulations which showed that this definition yielded more accurate results than others (such as using the panel *null point*).

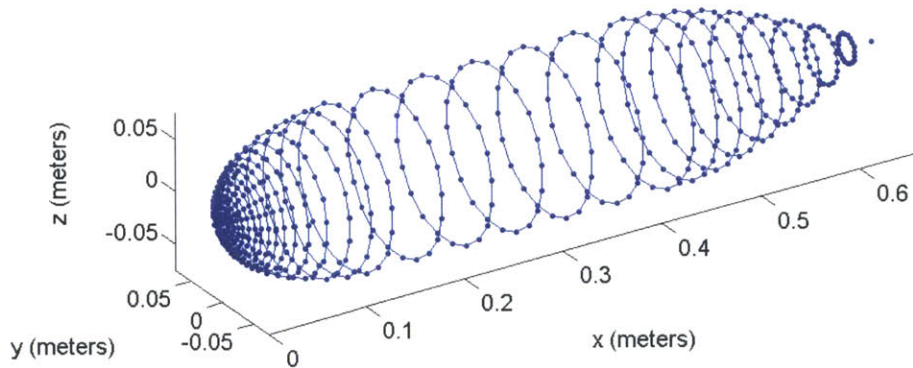


Figure 4-1: Diagram of the discretized vehicle. The circular vehicle cross-sections are highlighted, and each point represents a corner point. The panels can be visualized as the space between any four points.

4.2.3 Integration over source panels

Having defined the body discretization, the next step is to calculate the influence of each panel at every other panel's control point. These terms are known as the *influence coefficients*. It is clear that the exact influence of each panel cannot be calculated without knowledge of the source strength, which is of yet unknown. However, since the source strength over each panel is constant, it can be factored out of the integral equation, and the exact influence of each panel can be linearly scaled with source strength. As a result, the influence coefficients are defined as the influence of each panel, given a source strength $\sigma = 1$. With this definition, a straightforward matrix equation is formed which allows for the calculation of the actual source strengths. These actual strengths can later be multiplied by the influence coefficients to determine the contribution of each panel to the velocity potential or field.

The potential at an arbitrary point $P(x, y, z)$ due to a single panel can be given as:

$$\Phi(x, y, z) = \frac{-\sigma}{4\pi} \int_S \frac{dS}{\sqrt{(x - x_0)^2 + (y - y_0)^2 + z^2}} \quad (4.6)$$

This integration step requires some extra care, because each panel is fundamentally a 2D construct. As a result, the coordinates of each panel, and the point of interest, must be transformed into a panel-centered frame of reference for each set of calculations, with the following transformation matrix:

$$\mathcal{A} = \begin{bmatrix} u_1 & u_2 & u_3 \\ o_1 & o_2 & o_3 \\ n_1 & n_2 & n_3 \end{bmatrix}$$

Where $u_{1,2,3}$ are the components of one of the panel diagonals (normalized vector from one corner to the opposite corner), $n_{1,2,3}$ is the unit vector normal to the surface, and $o_{1,2,3}$ is the transverse unit vector (the cross product of \vec{u} and \vec{n}).

Therefore in (4.6), the coordinates x , y , and z are the transformed coordinates of the point of interest, and x_0 and y_0 represent the transformed coordinates of the panel's control point (typically $(0, 0)$). This geometry is illustrated in Figure 4-2.

Integration over the panel requires a lengthy process which is summarized by Hess and Smith [21]. Their derivation reduces the integral into a set of lengthy but closed

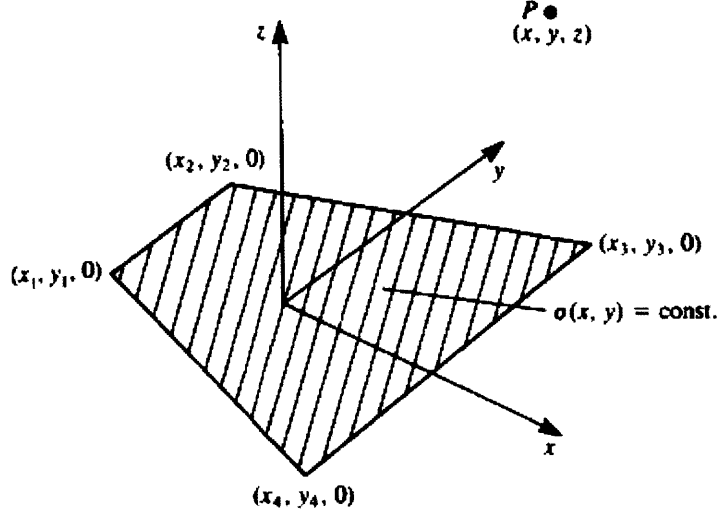


Figure 4-2: Diagram of the panel-centered frame of reference fixed to a quadrilateral constant-strength source element. The corners reflect the transformed coordinates of the corners (note that $z=0$), and P represents a point of interest. (adapted from Low Speed Aerodynamics, [27].

form equations for the induced potential at each control point due to each panel:

$$\begin{aligned}
\Phi = \frac{-\sigma}{4\pi} & \left(\left[\frac{(x-x_1)(y_2-y_1) - (y-y_1)(x_2-x_1)}{d_{12}} \ln \frac{r_1+r_2+d_{12}}{r_1+r_2-d_{12}} \right. \right. \\
& + \frac{(x-x_2)(y_3-y_2) - (y-y_2)(x_3-x_2)}{d_{23}} \ln \frac{r_2+r_3+d_{23}}{r_2+r_3-d_{23}} \\
& + \frac{(x-x_3)(y_4-y_3) - (y-y_3)(x_4-x_3)}{d_{34}} \ln \frac{r_3+r_4+d_{34}}{r_3+r_4-d_{34}} \\
& \left. \left. + \frac{(x-x_4)(y_1-y_4) - (y-y_4)(x_1-x_4)}{d_{41}} \ln \frac{r_4+r_1+d_{41}}{r_4+r_1-d_{41}} \right] \right. \\
& + |z| \left[\tan^{-1} \left(\frac{m_{12}e_1 - h_1}{zr_1} \right) - \tan^{-1} \left(\frac{m_{12}e_2 - h_2}{zr_2} \right) \right. \\
& + \tan^{-1} \left(\frac{m_{23}e_2 - h_2}{zr_2} \right) - \tan^{-1} \left(\frac{m_{23}e_3 - h_3}{zr_3} \right) \\
& + \tan^{-1} \left(\frac{m_{34}e_3 - h_3}{zr_3} \right) - \tan^{-1} \left(\frac{m_{34}e_4 - h_4}{zr_4} \right) \\
& \left. \left. + \tan^{-1} \left(\frac{m_{41}e_4 - h_4}{zr_4} \right) - \tan^{-1} \left(\frac{m_{41}e_1 - h_1}{zr_1} \right) \right] \right) \quad (4.7)
\end{aligned}$$

where

$$d_{12} = \sqrt{(x_2 - x_1)^2 + (y_2 - y_1)^2} \quad (4.8)$$

$$d_{23} = \sqrt{(x_3 - x_2)^2 + (y_3 - y_2)^2} \quad (4.9)$$

$$d_{34} = \sqrt{(x_4 - x_3)^2 + (y_4 - y_3)^2} \quad (4.10)$$

$$d_{41} = \sqrt{(x_1 - x_4)^2 + (y_1 - y_4)^2} \quad (4.11)$$

and

$$m_{12} = \frac{y_2 - y_1}{x_2 - x_1} \quad (4.12)$$

$$m_{23} = \frac{y_3 - y_2}{x_3 - x_2} \quad (4.13)$$

$$m_{34} = \frac{y_4 - y_3}{x_4 - x_3} \quad (4.14)$$

$$m_{41} = \frac{y_1 - y_4}{x_1 - x_4} \quad (4.15)$$

and

$$r_k = \sqrt{(x - x_k)^2 + (y - y_k)^2 + z^2} \quad k = 1, 2, 3, 4 \quad (4.16)$$

$$e_k = (x - x_k)^2 + z^2 \quad k = 1, 2, 3, 4 \quad (4.17)$$

$$h_k = (x - x_k)(y - y_k) \quad k = 1, 2, 3, 4 \quad (4.18)$$

The velocity influence coefficients (not to be confused with the potential influence coefficients) are given as:

$$u = \frac{\sigma}{4\pi} \left[\frac{y_2 - y_1}{d_{12}} \ln \frac{r_1 + r_2 - d_{12}}{r_1 + r_2 + d_{12}} + \frac{y_3 - y_2}{d_{23}} \ln \frac{r_2 + r_3 - d_{23}}{r_2 + r_3 + d_{23}} \right. \\ \left. + \frac{y_4 - y_3}{d_{34}} \ln \frac{r_3 + r_4 - d_{34}}{r_3 + r_4 + d_{34}} + \frac{y_1 - y_4}{d_{41}} \ln \frac{r_4 + r_1 - d_{41}}{r_4 + r_1 + d_{41}} \right] \quad (4.19)$$

$$v = \frac{\sigma}{4\pi} \left[\frac{x_1 - x_2}{d_{12}} \ln \frac{r_1 + r_2 - d_{12}}{r_1 + r_2 + d_{12}} + \frac{x_2 - x_3}{d_{23}} \ln \frac{r_2 + r_3 - d_{23}}{r_2 + r_3 + d_{23}} \right. \\ \left. + \frac{x_3 - x_4}{d_{34}} \ln \frac{r_3 + r_4 - d_{34}}{r_3 + r_4 + d_{34}} + \frac{x_4 - x_1}{d_{41}} \ln \frac{r_4 + r_1 - d_{41}}{r_4 + r_1 + d_{41}} \right] \quad (4.20)$$

$$\begin{aligned}
w = \frac{\sigma}{4\pi} & \left[\tan^{-1} \left(\frac{m_{12}e_1 - h_1}{zr_1} \right) - \tan^{-1} \left(\frac{m_{12}e_2 - h_2}{zr_2} \right) \right. \\
& + \tan^{-1} \left(\frac{m_{23}e_2 - h_2}{zr_2} \right) - \tan^{-1} \left(\frac{m_{23}e_3 - h_3}{zr_3} \right) \\
& + \tan^{-1} \left(\frac{m_{34}e_3 - h_3}{zr_3} \right) - \tan^{-1} \left(\frac{m_{34}e_4 - h_4}{zr_4} \right) \\
& \left. + \tan^{-1} \left(\frac{m_{41}e_4 - h_4}{zr_4} \right) - \tan^{-1} \left(\frac{m_{41}e_1 - h_1}{zr_1} \right) \right] \quad (4.21)
\end{aligned}$$

Following the calculation of the velocity coefficients, they must be transformed back into the inertial frame of reference. Typically, depending on the boundary condition enforced, only the potential influence coefficients *or* the velocity influence coefficients need to be calculated. For Dirichlet conditions, we calculate the first, and for the Neumann boundary condition we calculate the second.

4.2.4 Far-field approximation

The set of equations previously given are lengthy, and are generally completed at high computation cost. For improved computational speed, it is logical to implement an approximation when the point of interest P is far from the affecting panel. When the point of interest is approximately 3-5 panel lengths away from the panel, the panel can be accurately approximated as a single point source. With this, the potential influence is given as:

$$\Phi(x, y, z) = \frac{-\sigma A}{4\pi \sqrt{(x - x_0)^2 + (y - y_0)^2 + z^2}} \quad (4.22)$$

and the velocity influences are given as:

$$u(x, y, z) = \frac{\sigma A(x - x_0)}{4\pi [(x - x_0)^2 + (y - y_0)^2 + z^2]^{3/2}} \quad (4.23)$$

$$v(x, y, z) = \frac{\sigma A(y - y_0)}{4\pi [(x - x_0)^2 + (y - y_0)^2 + z^2]^{3/2}} \quad (4.24)$$

$$w(x, y, z) = \frac{\sigma A(z - z_0)}{4\pi [(x - x_0)^2 + (y - y_0)^2 + z^2]^{3/2}} \quad (4.25)$$

4.2.5 Reduction to linear problem and solution

Once the influence coefficients are calculated, they can be substituted back into the boundary value equation (4.5), providing an explicit equation to solve for the panel

source strengths. The boundary value equation can be rewritten, where the right hand side (giving normal velocities at panel control points) is represented as the matrix B_i , for $i = 1, 2 \dots N$ (where $N = 620$ panels):

$$\sum_{j=1}^N \sigma(\vec{\xi}, t) \int_{S_j} \frac{\partial}{\partial n(\vec{x}, t)} G(\vec{x}, \vec{\xi}, t) dS(\vec{\xi}, t) = B_i \quad (4.26)$$

The integral term in the left hand side represents the influence coefficients (of each panel j at each control point i), and we hereby represent it as the matrix P_{ij} , the *influence coefficient matrix*. This results in the final discretized matrix equation:

$$\sum_{j=1}^N \sigma_j P_{ij} = B_i \quad (4.27)$$

which is solved to obtain the source strengths of each panel, σ_j . These values are subsequently substituted back into equations (4.19) - (4.21) to solve for the fluid velocity at each control point, and into equation (4.17) to solve for the velocity potential at each control point. These terms can then be used in Bernoulli's unsteady pressure law to solve for the surface pressure:

$$P = -\rho \left(\frac{\partial \phi}{\partial t} + \frac{1}{2} |\nabla \phi|^2 + gz \right) \quad (4.28)$$

In (4.28), ρ is the water density, g is the gravitational acceleration constant, and z is the water depth at the point of interest.

While this method is straightforward to implement, special care must be taken in the case of rotating bodies or flows. In these cases, regardless of the reference frame chosen, it is required to update the surface normal velocity at each instant, which is a function of the oncoming flow and the body motion. In addition, for a dynamic system such as this one, the first term of Bernoulli's equation can no longer be ignored. It must be expanded to include the material derivative (because the points that we are interested in are on the surface of the vehicle, a material surface), and numerically computed for each timestep.

4.3 Simulated Results

4.3.1 Model verification

First, the source panel method was implemented on a 400 panel solid sphere in uniform flow, for which the analytical solution through potential flow is readily available:

$$\phi = U_\infty \cos \theta \left(r + \frac{a^3}{2r^2} \right) \quad (4.29)$$

$$v_\theta = -U_\infty \sin \theta \left(r + \frac{a^3}{2r^2} \right) \quad (4.30)$$

$$= -\frac{3U_\infty r}{2} \sin \theta \quad \text{when } a = r \quad (4.31)$$

The analytical solution to the velocity potential, and the comparison between the velocities calculated analytically and through the panel method over the surface of the sphere are shown in Figure 4-3. This serves to verify the accuracy of the simulation for a basic, static problem. Since there are no analytic solutions available for nonsymmetric rotating bodies, verification for the dynamic case must be performed by comparing simulated results to experimental data.

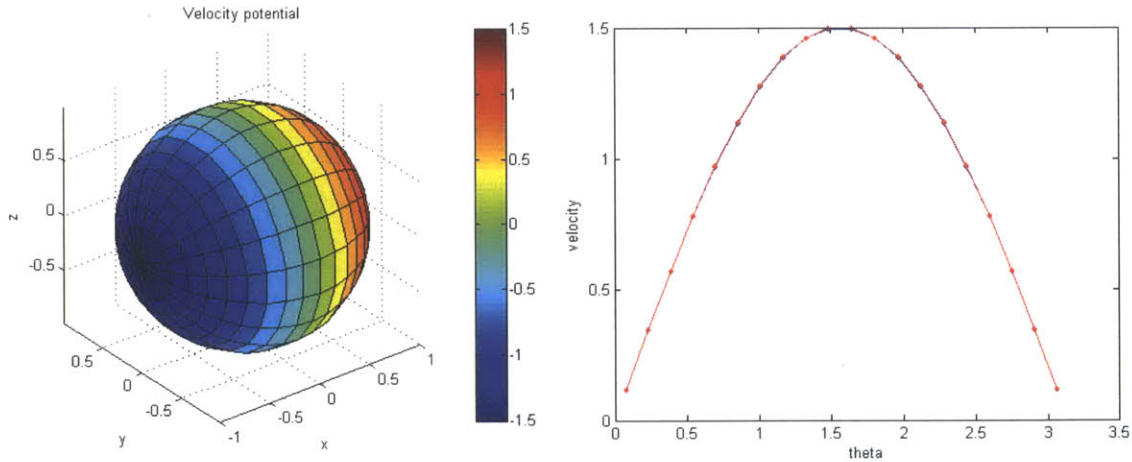


Figure 4-3: Left: The velocity potential calculated and plotted over the surface of a 400 panel sphere. Right: comparison between the analytical solution of velocity over the surface of the sphere and that calculated by the panel method.

4.3.2 Static pressure simulations

A number of simulations were performed to compute the pressure at the experimental sensor locations, for static tests (tests in which there is no acceleration of the vehicle). The computed surface pressures for these simulations was compared with experimental data collected previously (see Section 3.4). The results were additionally compared with a constant doublet panel method which was developed for the same vehicle. These comparisons show strong alignment between the source panel simulation and the experimental data (Figures 4-4, 4-5).

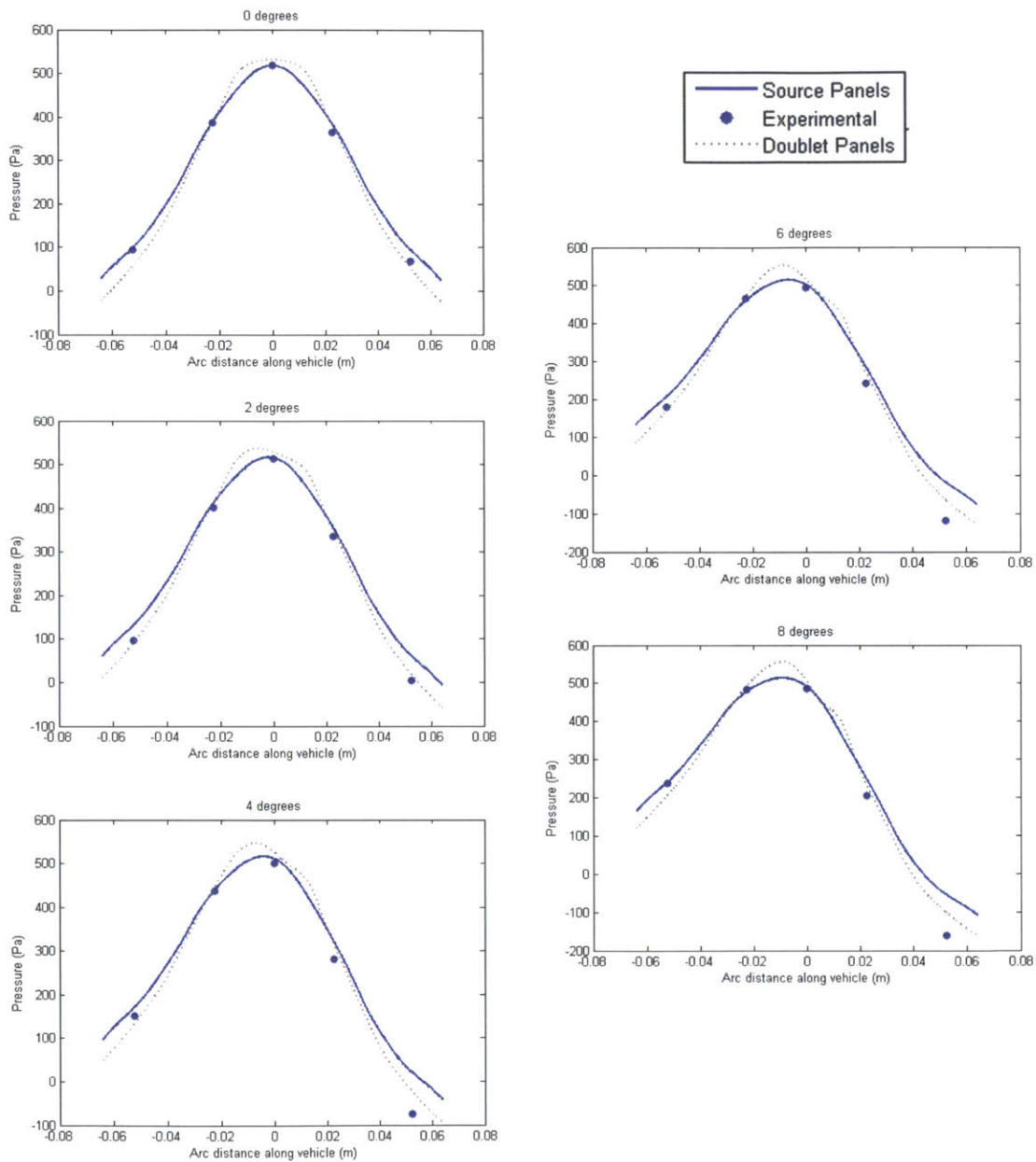


Figure 4-4: Comparison between the surface pressure simulated using the source panel method and the doublet panel method, compared with experimentally measured pressures.

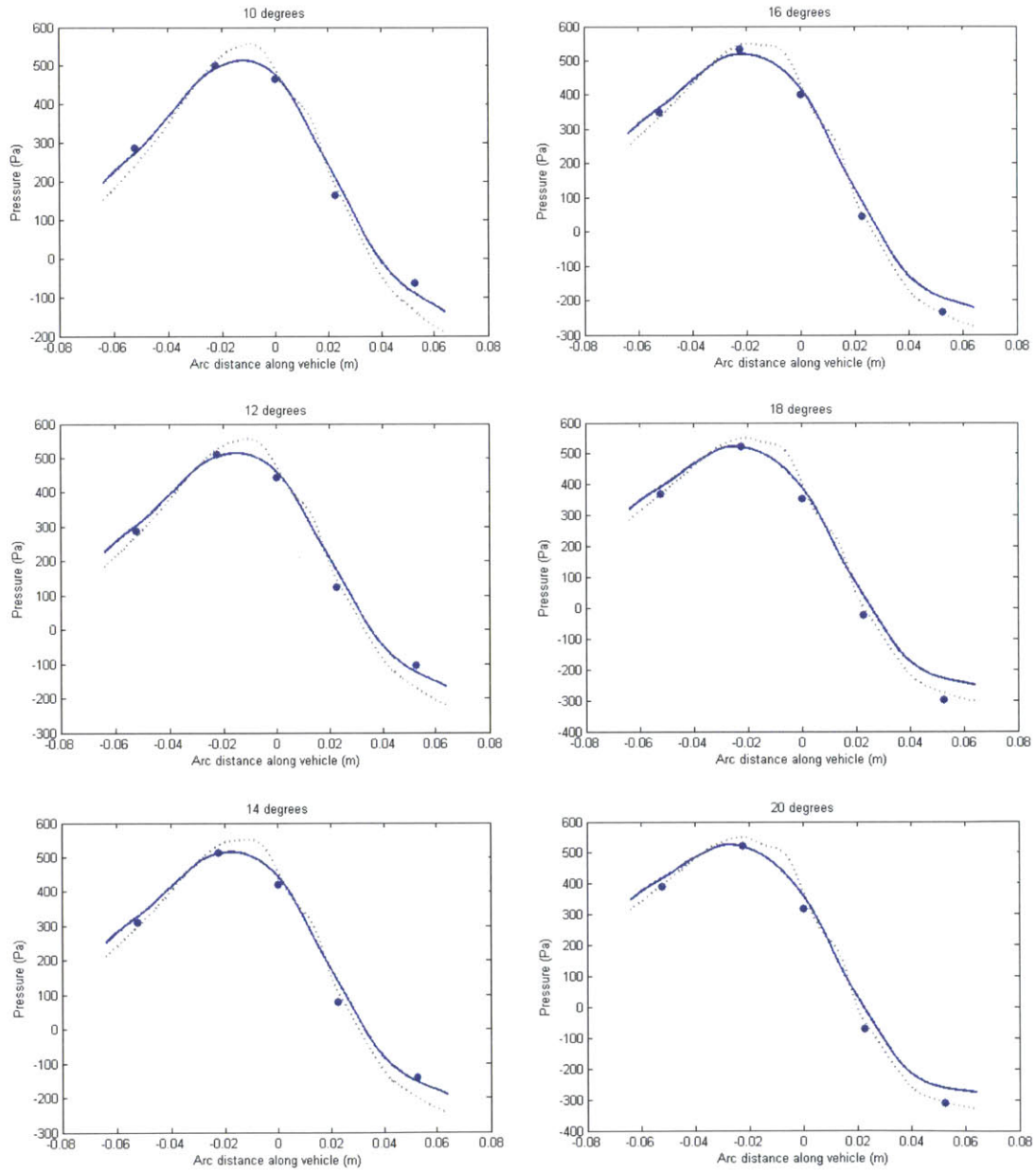


Figure 4-5: Comparison between the surface pressure simulated using the source panel method and the doublet panel method, compared with experimentally measured pressures.

They additionally show the superiority of the source panel simulation over the doublet panel simulation. Recall from equation 2.18 that the potential at any point of interest can be written in terms of two elementary solutions, the source and the doublet. Since the solution is not unique when both of these terms are included, the formulation may be split into formulations involving only one or both of those elements. However, the doublet panel method formulation involves an extra order of derivation of Green's function. Since Green's function goes as $1/r$, its second derivative goes as $1/r^3$, which becomes an increasingly small term as the size of the panels is reduced. These small terms result in very poor conditioning of the influence coefficient matrix, which in turn causes some computational error when the panels are small, or the size of the panels changes suddenly. Since the size of the panels decreases near the nose of the vehicle, the error is much higher for the doublet panel method in this region. The solutions they yield are also less smooth than those produced by the source panel method, for the same reasons. However, for points of interest farther back from the nose, the doublet panel method may be more accurate.

However, since the region of interest is the front of the vehicle, the source panel method was chosen for its higher accuracy and smoothness in this region.

4.3.3 Dynamic pressure simulations

Following this verification that the panel method was capable of simulating experimental pressures measured at static angles, several simulations were performed to visualize the pressure field over the surface of the vehicle during a high speed turn. For these simulations, it became extremely important to ensure that a) the dynamic boundary conditions were met, since the surface velocity is now a function of both the oncoming velocity and the velocity induced from turning, and b) Bernoulli's equation was properly implemented to account for the appropriate velocity and potential terms.

With these conditions ensured, the pressure field throughout several high speed turns was simulated. The results of one of these simulations is displayed in Fig. 4-6.

In Figure 4-6, red indicates high pressure and blue indicates low pressure. In particular, note how the high pressure region shifts first to one side and finally settles on the other side at the front of the vehicle. This initial shift of the high pressure region is exactly the pressure undershoot that we previously saw in the experimentally measured pressure traces during maneuvers. These simulations aided in visualization of the added mass effects which arise during vehicle maneuvers.

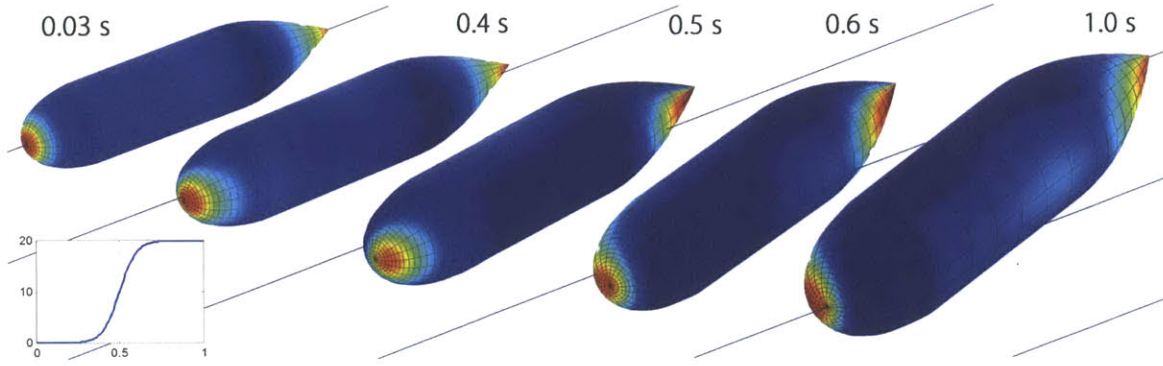


Figure 4-6: The pressure field over the surface of the vehicle as it turns from 0 to 20 degrees, with the profile of the turn shown in the lower left hand plot. The diagonal lines in the background show the direction of the oncoming flow.

By collapsing the simulation data over an entire turn into one plot, the pressure over the entire vehicle, over time, can be visualized and compared more effectively for different turns. To illustrate this, Figure 4-7 shows the vehicle pressure profiles for a) a turn performed at constant velocity, b) a turn performed with slow acceleration, and c) a turn performed with faster acceleration.

In Figure 4-7, the lower panel numbers correspond to panels at the front of the vehicle, and higher numbers correspond to the panels near the end. Each chord on the vehicle contains 20 panels, so the first 20 panels are at the same longitudinal position, the second 20 panels are at the same longitudinal position, and so on. This results in the ridge-like appearance of the map. The peaks in the ridges correspond to the sensor points along the plane of turning (on the left and right sides of the vehicle, in this case). The turn itself occurs around 0.5 seconds, and so the greatest changes in pressure along the entire vehicle occur around the center of the time axis.

From these plots, it can be seen that for certain panels on the vehicle, the NMP-like response during turning maneuvers is much more evident. This indicates that placing pressure sensors on different sections of the vehicle could act to provide very different kinds of information. Sensors near the peak in the front of the vehicle may provide more information on the angle of flow, while sensors placed just behind them may provide the most information on yawing acceleration. It also becomes clear that the sensors located along the plane of turning will experience the greatest pressure changes, so in a 3D environment, placing sensors in a ring around the vehicle would allow for a simple way of detecting the direction of turning. To analyze the fast acceleration case a little more closely, the pressure which would be expected at a static angle of attack was subtracted from the pressure map. The remainder is then the

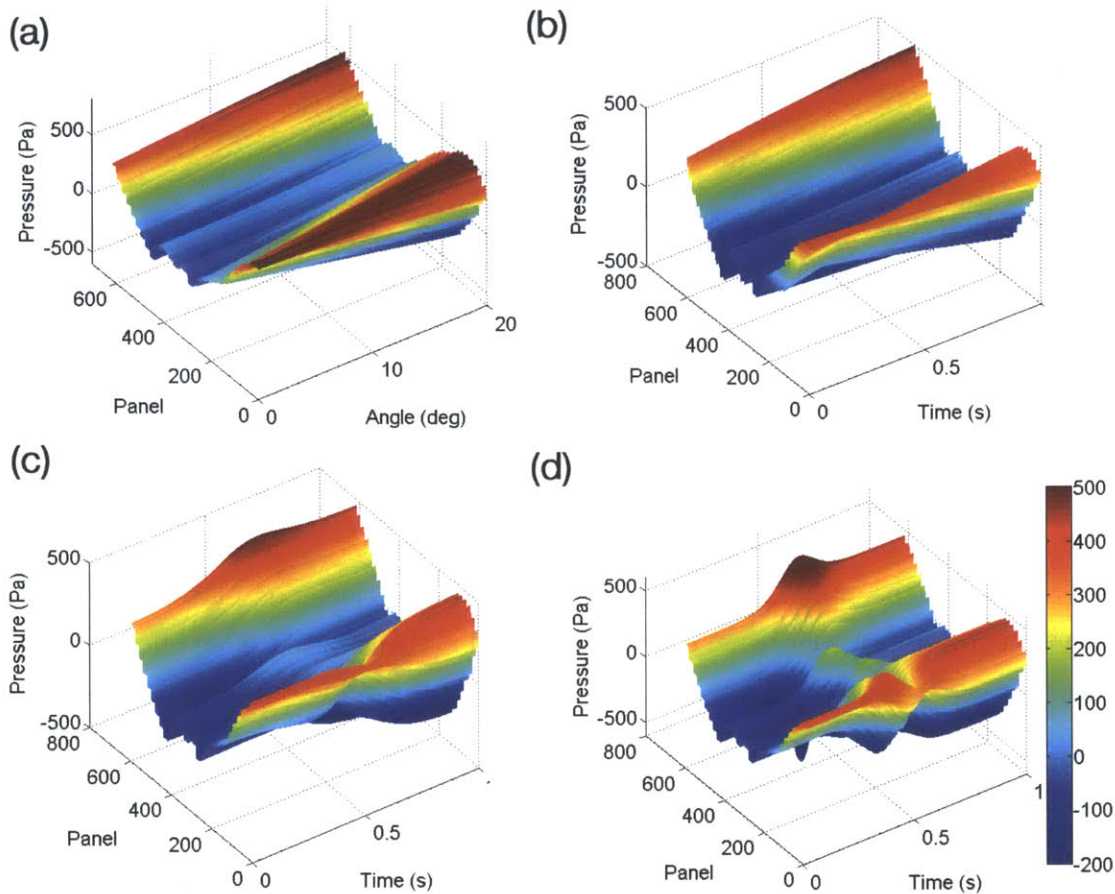


Figure 4-7: Pressure plotted against time and space (panel of the vehicle) for a) static pressure only (no turning), b) a constant velocity turn, c) a slowly accelerating turn, and d) a faster turn.

dynamic pressure alone, which is the component which is dependent on acceleration and therefore a result of added mass effects. This is plotted for only the left and right sensors in Figure 4-8.

In this figure, the effect of the accelerating turn at various longitudinal positions of the vehicle is clear. Due to the slight lateral offset of the rotational center, the map is not as symmetric as one would expect. Visualizing the dynamic pressure in this way allows for analysis of sensor locations for ideal feedback. For this particular turn, sensors located between chords 6 and 15 would be well placed. This happens to correlate well with the sensor locations in our physical model, which are at chords 4 and 9. For implementation on a physical system, these types of simulations could help to inform choice of sensor placement, which could be based on expectations of

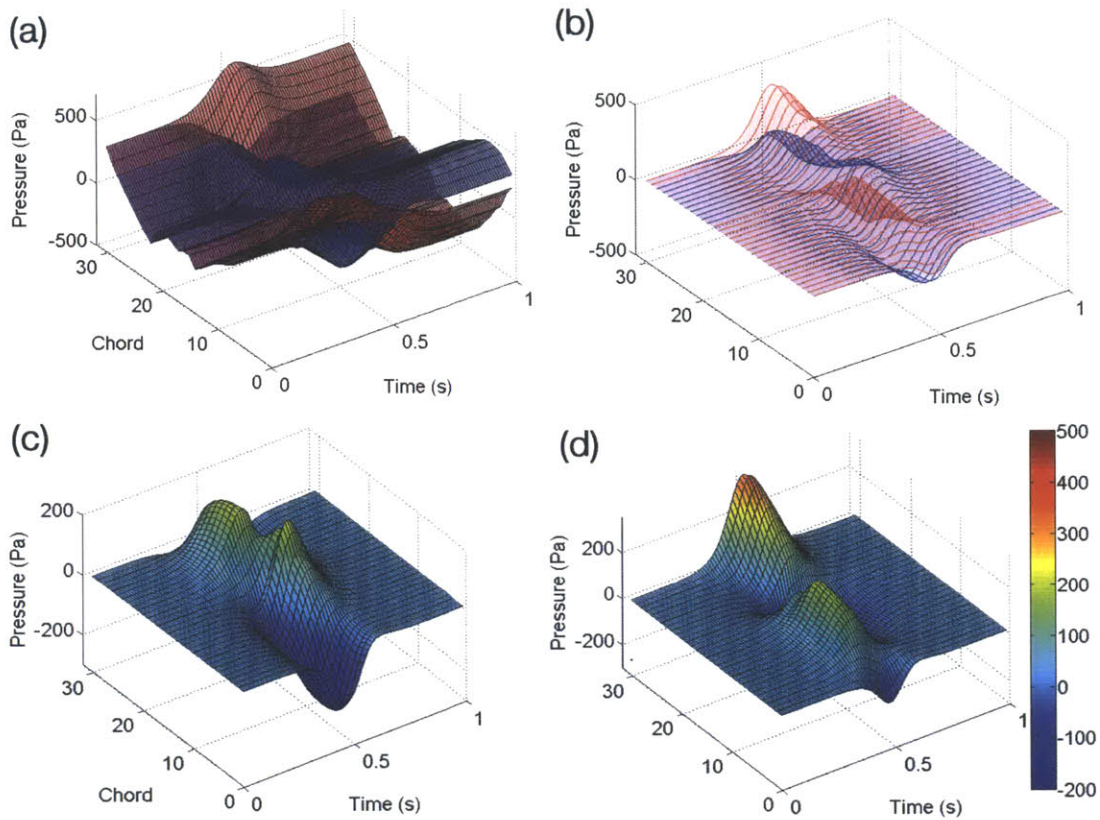


Figure 4-8: Pressure plotted against time and space for the fast turn. a) pressure outline for both sides of the vehicle during the turn. b) dynamic pressure outline for both sides of the vehicle during the turn. c) dynamic pressure measured at only the left sensors. d) dynamic pressure measure at only the right sensors.

turning rate and the expected frequency of changes in surrounding flow.

4.3.4 Dynamic pressure verification

As previously shown, simulations conducted at static angles of attack and constant oncoming flow velocity (1 m/s) matched experimental data very well. However, the more interesting case is that of the vehicle executing dynamic maneuvers, and to validate the model for these cases, a set of experiments and simulations were conducted with the vehicle performing turns at varying rates. Fig. 4-9 shows the strong consistency between the experimental and simulated pressure measurements for a turn to 16 degrees and back to 0 degrees. The nonlinear pressure fluctuations during the turns are well captured by the simulation. The oscillations seen in the measurements are a result of mechanical vibrations during the experiment. The full set of these simulations (additional examples available in Appendix A) served to sufficiently validate the accuracy of the system model, a requirement for good observer and controller performance.

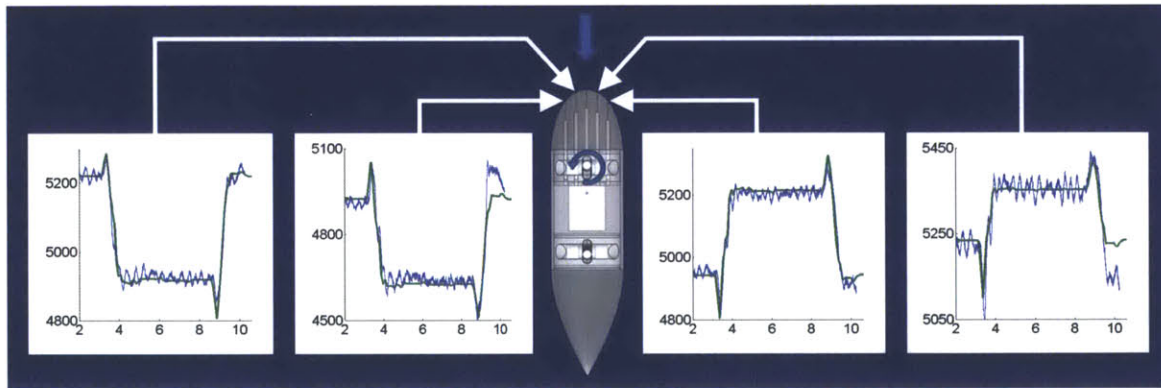


Figure 4-9: Simulated (green) and experimentally measured (blue) pressure observed at 4 pressure sensors during a turn from 0 to 16 degrees and back to 0 degrees. Pressure (Pa) is plotted against time (s). The blue arrow represents the direction of oncoming flow.

Chapter 5

Kalman Filter Inverse Modeling

While we now have a model which is capable of calculating the surface pressure values that would be expected for specific states or scenarios, this cannot be directly incorporated into a control system. A classical control system operates on the difference between a desired state and the current state, and this is as yet unknown. However, given the input and output of the real system, a state observer can reproduce the system's internal states. Within this system, the primary state of interest is the yaw angle, the inputs are any torques produced by the vehicle, and the outputs are the pressure measurements.

5.1 The Kalman Filter

The Kalman Filter is an optimal observer, which recursively estimates the state of a system or process in a way that minimizes the mean squared error. It is unique among filters in being a purely time-domain filter, requiring only the previous state estimate and the current measurement at each time step. The standard Kalman Filter requires the state transition and observation models of the system, which must be represented in linear matrix form.

Estimation for nonlinear systems is much more difficult. The optimal solution requires propagation of the full probability density function, which cannot generally be described using a finite number of parameters. As a result, approximations must be made, and the choice of the correct approximation is not always simple. Many different approximations have been developed, but most are complex and limited to very specific types of systems. The Kalman Filter, on the other hand, only uses the first two moments of the state in its update rule, which is a comparatively simple representation. However, this well bounded representation has a number of benefits

which makes the KF a very powerful and versatile tool for nonlinear estimation as well as linear estimation.

For nonlinear systems, a few modifications must be made to the standard Kalman Filter to allow for its use with nonlinear equations which do not possess a constant state transition matrix. In the Extended Kalman Filter (EKF), Jacobian matrices are produced as a linearized representation of the non-linear functions around the current estimate. These Jacobian matrices can then be used in place of the linear transformations of the standard KF. However, this approach suffers a number of drawbacks. First, the linearized transformations only work well when the error propagation can be well approximated by a linear function. For instance, if the relationship between state and output is extremely nonlinear or discontinuous, a small error in the state could cause a massive error in the output. In this scenario, the EKF would be a poor estimator, because the estimate could diverge completely. Secondly, the necessity for calculating Jacobian matrices implies that the nonlinear functions must be smooth. As a result, for any functions that are discontinuous at any points, an EKF would not work. Finally, the calculation of Jacobian matrices can be a difficult process that is computationally taxing and error-prone. This makes it difficult to program and difficult to debug.

An alternative to the EKF is the Unscented Kalman Filter (UKF). The UKF uses a deterministic sampling technique known as the *unscented transform*, which operates on the idea that a probability distribution is easier to approximate than an arbitrary nonlinear function [26]. In contrast to the EKF, which applies an approximation to the nonlinear function and uses that to operate on partial distribution information (mean and covariance), the UT uses the exact nonlinear function to operate on an approximating probability distribution.

Within this approach, a number of *sigma points* which encode the known mean and covariance are first selected around the estimated state. These sigma points are then each propagated through the exact nonlinear state transition and observation functions, to yield a transformed ensemble with some new mean and covariance. By using the exact nonlinear transformation on a set of points with a given distribution, we can capture a set of known statistics of an unknown distribution. This allows for the propagation of mean and covariance information, resulting in greater accuracy and ease of implementation, with the same order of calculations as the EKF. In addition, by eliminating the need for linearization, the UKF is capable of being used on any nonlinear function, including discontinuous ones.

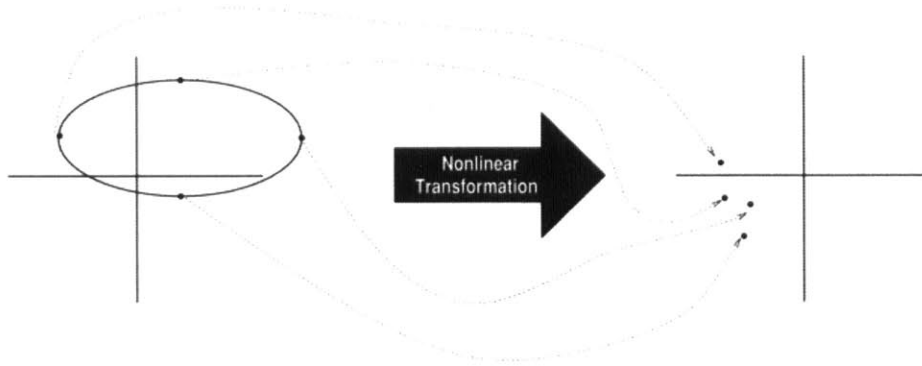


Figure 5-1: A diagram illustrating the principle of the unscented transformation. Instead of propagating a single state estimate through a linearized function, a set of sigma points are propagated through the exact nonlinear function.

5.2 Applying the UKF to Estimate Yaw Angle

Within this application, an Unscented Kalman Filter is used to estimate the system states (yaw angle θ and yaw rate $\dot{\theta}$), given four pressure measurements from the surface of the vehicle. The generalized state transition model is written as:

$$\vec{x}_{k+1} = f[\vec{x}_k, \vec{u}_k] + \vec{w}_k \quad (5.1)$$

Where \vec{x} is the vehicle state, k is a discrete timestep, f is the nonlinear state transition function, \vec{u} is the control input, and \vec{w} is the process noise associated with the system. For this system, the explicit state transition model is:

$$x_{1,k+1} = x_{1,k} + x_{2,k} \cdot dt \quad (5.2)$$

$$x_{2,k+1} = x_{2,k} + \left(\frac{\tau}{J + m_{66}} - \frac{x_{2,k}}{J + m_{66}} U m_{66} \cos x_{1,k} - \frac{1}{2(J + m_{66})} (m_{22} - m_{11}) \sin 2x_{1,k} \right) \cdot dt \quad (5.3)$$

Where x_1 is the yaw angle θ , x_2 is the yaw rate $\dot{\theta}$, τ is the model abstraction representing the amount of torque output by deliberate vehicle actuation, and dt is the time elapsed since the last measurement update. J , m_{66} , m_{11} , and m_{22} are the

inertial and added mass vehicle parameters estimated as:

$$\begin{aligned} m_{11} &= 0.927 \text{ kg} \\ m_{22} &= 9.12 \text{ kg} \\ m_{66} &= 7.17 \cdot 10^{-2} \text{ kg} \cdot \text{m}^2 \\ J &= 0.627 \text{ kg} \cdot \text{m}^2 \end{aligned}$$

These are estimated from the vehicle geometry and the slender body approximation, as defined by Newman [36].

As such, this model accounts for motions resulting from a known control effort, as well as added mass effects from known vehicle motion, but it does not account for the unknown disturbances to vehicle angle or external current. A slightly improved model which also takes into account the dynamics of helical vortices that form at the back of the vehicle during turns can be formulated as described by Hoerner [23].

The generalized observation equation is:

$$\vec{z}_k = g[\vec{x}_k] + \vec{v}_k \quad (5.4)$$

Where \vec{z} is the vector of the pressure measurements, g is some nonlinear transformation, and \vec{v} is the vector of associated measurement noises. The explicit observation model is more complex; it incorporates the panel method system model previously derived, which produces a set of pressure measurements, given the system state and relevant parameters. Presently, the importance of an accurate system model becomes apparent. Since the state transition model is incapable of modeling disturbances to the system, the measurements will be fully responsible for capturing their effect, and the panel method model must then accurately decipher the pressure measurements in producing a corrected estimate.

The following UKF procedure is adapted from Julier [26].

First, a symmetric set of $2N$ sigma points with mean \bar{x} and covariance P is generated, which we denote χ :

$$\chi_i = \bar{x} + (\sqrt{N_x P_x})_i \quad i = 0, \dots, n \quad (5.5)$$

$$\chi_{i+n} = \bar{x} - (\sqrt{N_x P_x})_i \quad i = 0, \dots, n \quad (5.6)$$

Where each point has even weight:

$$W = 1/2N_x \quad (5.7)$$

The second term in equation (5.5) represents the i th row or column of the matrix square root of $N_x P_x$, the original covariance matrix multiplied by the number of dimensions.

Different formulations for generation of the sigma points is available, depending on the properties of the true distribution. In general, if the skew of the distribution is zero, then a symmetric set, such as the set of $2N$ points, is more accurate because the odd moments will be zero. If the skew of the true distribution is nonzero, then another set, such as the simplex set [26], may produce better results.

Once a set of sigma points is generated, each of the sigma points is then instantiated through the process model (5.1) and observation model (5.4), using the standard unscented transformation. This produces the *a priori* state estimate \hat{x}_k and the estimated measurement \hat{z}_k .

The innovation covariance (covariance of predicted measurements) is calculated as:

$$P_k^z = \sum_{i=0}^p W^{(i)} (\hat{z}_k^{(i)} - \hat{z}_k) (\hat{z}_k^{(i)} - \hat{z}_k)^T \quad (5.8)$$

Where p is the number of sigma points and $W^{(i)}$ represents the weight of each. The *a priori* state covariance matrix is:

$$\hat{P}_k = \sum_{i=0}^p W^{(i)} (\hat{x}_k^{(i)} - \hat{x}_k) (\hat{x}_k^{(i)} - \hat{x}_k)^T \quad (5.9)$$

And the cross covariance matrix is given as:

$$P_k^{xz} = \sum_{i=0}^p W^{(i)} (\hat{x}_k^{(i)} - \hat{x}_k) (\hat{z}_k^{(i)} - \hat{z}_k)^T \quad (5.10)$$

These are used to update the state using the normal Kalman filter update equation:

$$x_k = \hat{x}_k + K_k (z_k - \hat{z}_k) \quad (5.11)$$

Where z_k is the vector of actual measurements, and K_k is the Kalman gain matrix, given by:

$$K_k = P_k^{xz} (P_k^z)^{-1} \quad (5.12)$$

The *a posteriori* covariance matrix is:

$$P_k = \hat{P}_k - K_k P_k^z K_k^T \quad (5.13)$$

The state estimate (5.11) and the covariance (5.13) are updated at each timestep, given the new set of pressure measurements. In this manner, the UKF is run recursively to constantly update the state estimate, provided new measurement information.

In applying this filter, we make the assumption that the oncoming flow velocity is a constant 1 m/s, to reduce the order of the system at hand. However, the Kalman

Filter could easily be extended to estimate flow velocity and acceleration as additional states.

5.3 Results from UKF Implementation

A key balance exists between the process and measurement noise covariance matrices in the UKF. Fundamentally, the Kalman Filter attempts to optimize its dependence on the state transition model and the measurement model based on the estimated noise covariance in each. As a result, the values of these matrices largely drive the convergence of the system. Simulations were conducted to test the effect of varying these parameters, and the results of these are shown in Appendix B.

For the final filter, the process (Q) and measurement (R) noise covariance matrices used were:

$$Q = \begin{bmatrix} 0.5 & 0 \\ 0 & 0.25 \end{bmatrix} \text{ deg, deg/s} \quad (5.14)$$

$$R = \begin{bmatrix} 3 & 0 & 0 & 0 \\ 0 & 3 & 0 & 0 \\ 0 & 0 & 3 & 0 \\ 0 & 0 & 0 & 3 \end{bmatrix} \text{ Pascals} \quad (5.15)$$

The measurement noise covariance matrix was chosen to closely reflect the amount of measurement noise observed in experiments. However, as there is not a good way to estimate the magnitude of process noise in the system, various values were tried, and the final values were chosen based on desired observer response. Changing these parameters can affect the UKF performance substantially. Typically, overestimation of the measurement noise results in less oscillation of the estimate, but more delay in convergence. When the estimated process noise is inaccurate, the estimated angle experiences some delay or simply does not converge to the actual angle.

The application of the UKF with the parameters shown yields a reasonably accurate estimate, with oscillations about the actual state on the order of the measurement noise, as predicted (Fig. 5-2). These oscillations could be filtered out to some extent with an additional low-pass filter for a smoother overall estimate. A smoother estimate would improve robustness and stability when the estimate is used in conjunction with a PID controller for system control.

Fig. 5-2 shows a comparison between the estimate the UKF is capable of producing and the estimate which was used with the Braitenberg controller described previously.

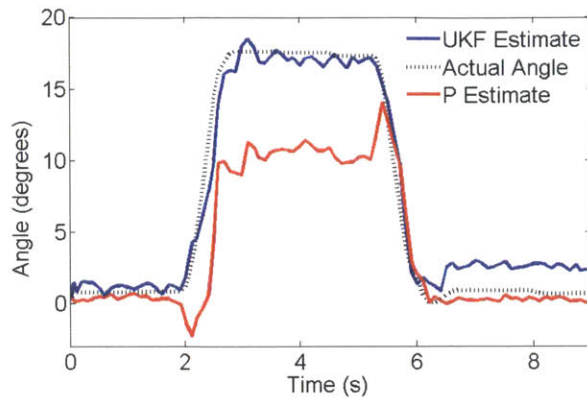


Figure 5-2: A comparison between the actual angle the vehicle is at during an experiment, the estimated angle as produced by the Unscented Kalman Filter, and the estimated angle as produced by the proportional estimator.

Due to the nonlinear nature of the system, the gain which must be applied to the system at a static yaw angles varies with the angle. As the angle increases, the gain must increase as well. This results in higher deviations of the estimate as the yaw angle grows larger. Furthermore, with the proportional estimator, the dynamic responses observed in the pressure during sudden turns results in an initial undershoot behavior, as can be seen. The UKF is able to resolve both of these issues.

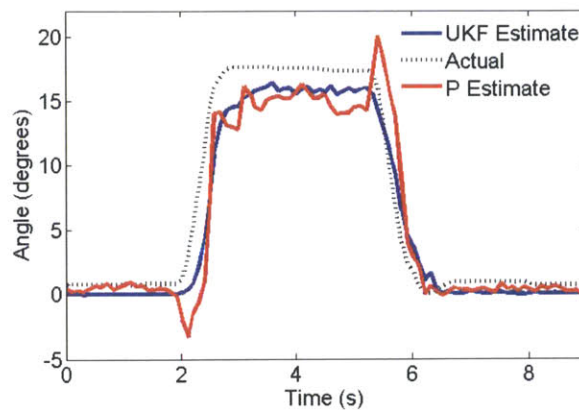


Figure 5-3: A comparison between the actual angle the vehicle is at during an experiment, the estimated angle as produced by the Unscented Kalman Filter, and the estimated angle as produced by the proportional estimator.

Fig. 5-3 shows a simulation conducted with a different set of parameters:

$$Q = \begin{bmatrix} 1 & 0 \\ 0 & 1 \end{bmatrix} \text{ deg, deg/s} \quad (5.16)$$

$$R = \begin{bmatrix} 3 & 0 & 0 & 0 \\ 0 & 3 & 0 & 0 \\ 0 & 0 & 3 & 0 \\ 0 & 0 & 0 & 3 \end{bmatrix} \text{ Pascals} \quad (5.17)$$

In addition, a higher gain was applied to the estimate from the Braitenberg controller. With this higher estimate of process noise covariance, it can be seen that oscillation of the estimate is largely reduced, but a large time lag is also introduced, and the estimate does not completely converge to the actual state. The time lag is on the order of the lag introduced by the proportional estimate. However, the UKF estimate here contains far less noise, and eliminates the undershoot behavior observed previously. This shows that the use of this observer in a model-based controller would improve the stability of the system, even if it were not able to eliminate the lag in response.

Through additional simulations, we also demonstrate that the noise in the estimate can be reduced by the use of additional sensors, as is expected.

Chapter 6

Summary and Conclusions

In this work, we have drawn inspiration from nature's blind cavefish to develop an underwater sensor which could supplement traditional vision and sonar systems to aid AUVs, particularly in dark or murky environments. This project has demonstrated one application, the active detection and correction of a vehicle's yaw angle. We have shown that potential flow can be used to simulate the flow field around the head of an underwater vehicle accurately, and moreover, we have demonstrated the application of this basic and well-studied method of simulation as the basis for a state estimator which can accurately assess the vehicle's current yaw angle, despite dynamic maneuvering and changes in flow. This state estimator is critical to the development of a control system which would be capable of maintaining the vehicle orientation at some desired value.

In the first phase, a towed underwater vehicle was constructed and equipped with 5 frontal pressure sensors. A number of experiments were conducted at static sideslip angles in order to inform a lookup table which could be used in control system development. However, it was quickly noted that dynamic changes in the flow, due to vehicle maneuvers or outside disturbances, caused added mass effects which produced large and unexpected undershoot behavior in the pressure signals. This NMP-like behavior was observed to cause delays in system response, as well as instability when high gains were applied within a proportional feedback control system. As a result, it was determined that a model-based controller would be necessary for improved response.

A model-based controller is constructed from two parts: a system model which can accurately simulate surface pressure given the system state, and an inverse model which can accurately estimate system state provided several pressure measurements. The first element was developed using a first-order 3D Rankine source panel method,

in which the vehicle was simulated as a construct of 620 constant source panels. Simulations were first conducted to show that the model accurately simulated the 5 relevant pressure measurements for the static angle experiments previously conducted. Then, additional simulations were conducted to demonstrate that the model was capable of accurately predicting the pressure traces measured during turns at various speeds. These simulations exhibited the ability of the model to simulate both static and dynamic surface pressure, provided the system state.

The second element of the model-based controller was constructed using an Unscented Kalman Filter. The UKF is an optimal estimator which uses the system model to estimate the expected pressures given an estimated state. It then compares the estimated pressures with the actual measured pressures and uses a least-squares technique to correct the state estimate. This inverse model was found to be capable of estimating the state with much higher accuracy than an estimator based on only the relationship between static angle and pressure. However, the oscillations in the estimate are high - on the order of the measurement noise within the system. This is expected, because the state transition model within the UKF does not account for disturbances, which are unpredictable. However, the oscillations can be reduced by the installation of a greater number of sensors.

The final state estimation algorithm requires solving the system model at every timestep, which is a lengthy process due to the order of the panel method simulation. As a result, it was not able to be incorporated into a real-time control system. However, there are several measures which could be taken to reduce to the computation time necessary, and these are discussed in Chapter 7. However, the basic idea of using a panel method to inform a control system is very powerful, and with the necessary corrections, could be the basis for a feedback control system which is capable of responding to highly nonlinear and unpredictable state changes. An enhanced control system developed around this concept would be faster and more robust to disturbances in flow and dynamic maneuvers.

This project has demonstrated the feasibility of using an ALL in one application - the detection and correction of a vehicle's yaw angle. In particular, it has shown that an exceptionally simplistic and low-cost sensing system inspired by a fish's cranial lateral line is capable of producing fast feedback, which can be used, with an understanding of hydrodynamics, to control an underwater vehicle. Additional research in the hydrodynamic theory surrounding fluid motion around objects, in wakes, and in dynamic environments can be used to inform control systems for a variety of tasks for future AUVs.

Chapter 7

Recommendations for future work

There are several key areas for improvement within this project. The biggest obstacle lies in solving the system model faster. In fluid dynamics, the structure and characteristics of the flow are governed by a complex set of equations which are fundamentally nonlinear and very difficult to solve. Even the most advanced computational methods are generally slow, and there is a high tradeoff between speed and accuracy. For control of an underwater system, speed is required for both real-time operation and stability, but accuracy is also required for good estimation and stability. Within this project, it has been shown that even for a system model which implements a number of simplifying assumptions, and reduces the system to a 2-dimensional system to solve, the solution is still obtained too slow for real-time operation. However, there are a number of ideas to try in improving the speed of computation.

7.1 Optimization of the panel method

As the goal of this project was to construct a methodology for development of a control system, as opposed to optimizing the parameters at each step, many of the parameters used could still be optimized. First, the number of panels chosen to represent the vehicle (620) was chosen arbitrarily with the goal of producing a reasonably smooth representation, which it did. However, reduction in the panel number can drastically reduce the number of computations to be performed at each timestep, since the number of calculations goes as $\mathcal{O}[N^2]$ (where N is the total number of panels). Experiments could be conducted to determine the tradeoff between accuracy of the pressure simulated at the relevant locations and the number of panels used. Since the region of interest is the front of the vehicle, modeling the back with fewer panels would likely cause minimal error to the solution.

Secondly, due to the smooth and simplistic geometry of the vehicle, it is possible that modeling the system as a 2D system would still provide a good basis for the UKF. This would reduce the problem to a 1D problem and reduce the number of calculations even further. Simulations could be conducted to determine if this is a possible alternative.

7.2 Physics-based learning model

Another way to improve the speed of state estimation for implementation in a real-time control system is to use a physics-based learning model (PBLM) [43]. A physics-based learning model provides a framework in which intermediate models are used to capture important physical aspects of the problem, and these aspects are incorporated into generic learning models. This hybrid of a pure physics-based model (which is what was used in this project) and a learning-based model results in a model which is capable of producing solutions quickly and relatively accurately. Its use has been successfully demonstrated on ship hydrodynamics problems, and was shown to possess higher prediction accuracy than generic learning models, and to be orders of magnitude faster than high-resolution CFD. This may be a promising avenue to explore for real-time control systems pertaining to fluid flows.

7.3 Development of real-time control system

Finally, if the state estimator can be improved to operate in real-time, a control system could be developed for implementation on a physical system. Important aspects to test would be robustness of the system to disturbances or turbulent flows, and operation of the system in environments with changing flows, such as in the wake of an object in oncoming flow.

Appendix A

Additional Dynamic Pressure Simulations

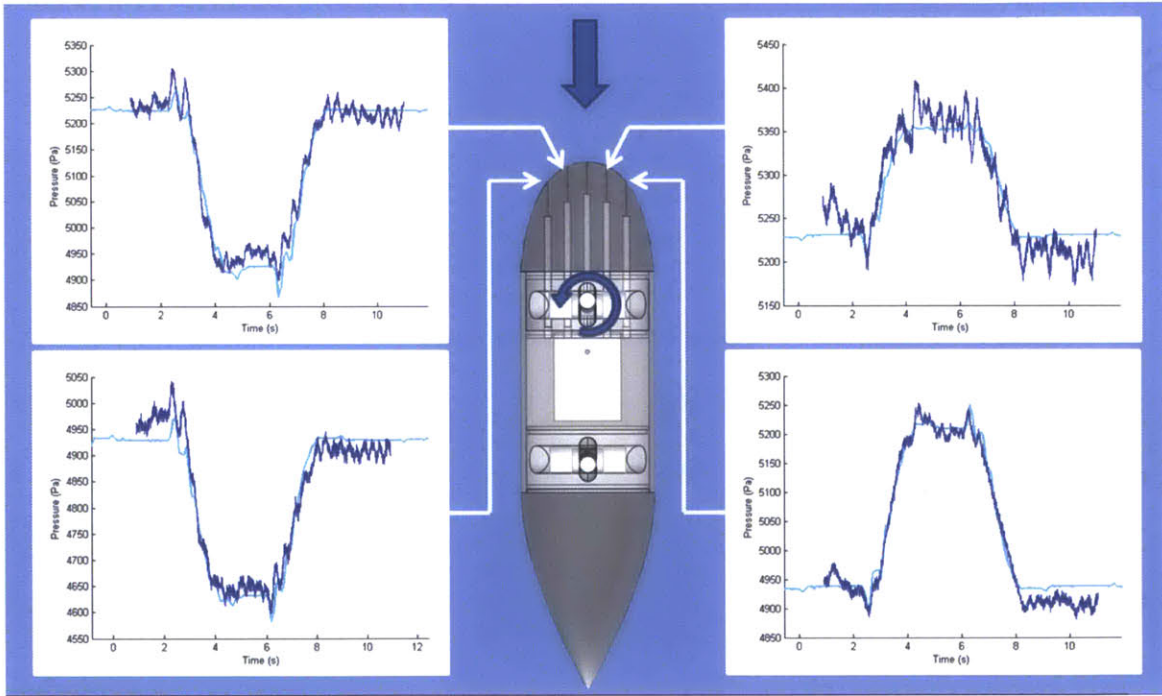


Figure A-1: Simulated (cyan) and experimentally measured (blue) pressure observed at 4 pressure sensors during a turn from 0 to 16 degrees and back to 0 degrees, with maximum acceleration of $13 \text{ deg}/s^2$. Pressure (Pa) is plotted against time (s). The blue arrow represents the direction of oncoming flow.

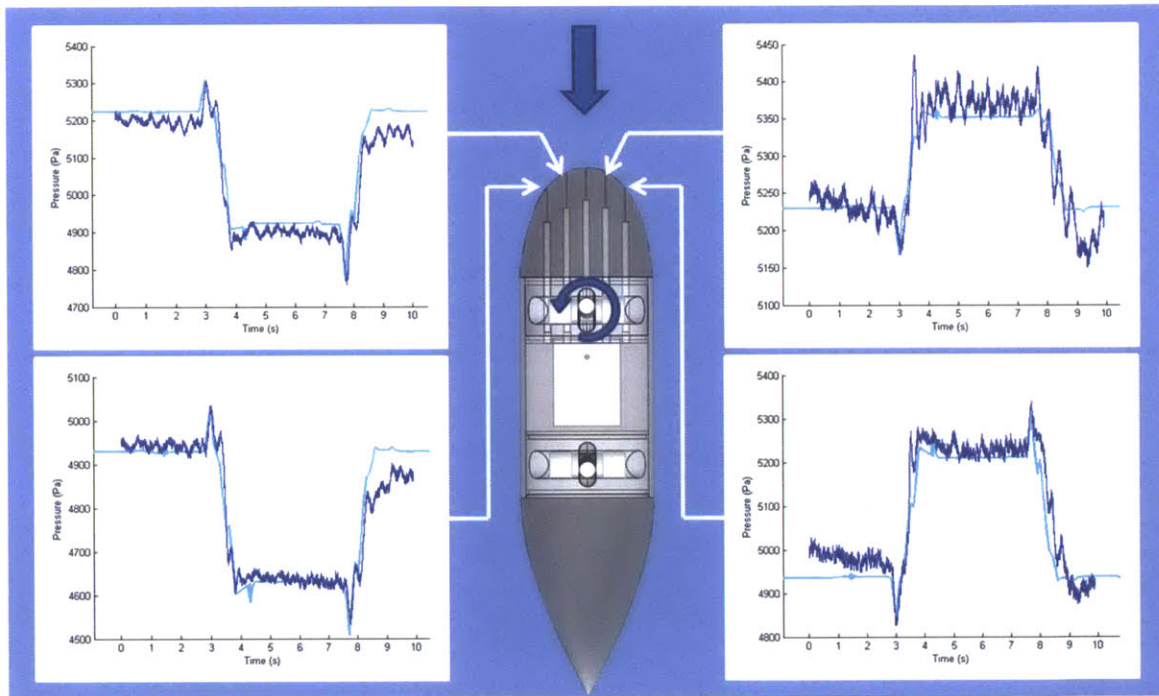


Figure A-2: Simulated (cyan) and experimentally measured (blue) pressure observed at 4 pressure sensors during a turn from 0 to 16 degrees and back to 0 degrees, with maximum acceleration of 46 deg/s^2 . Pressure (Pa) is plotted against time (s). The blue arrow represents the direction of oncoming flow.

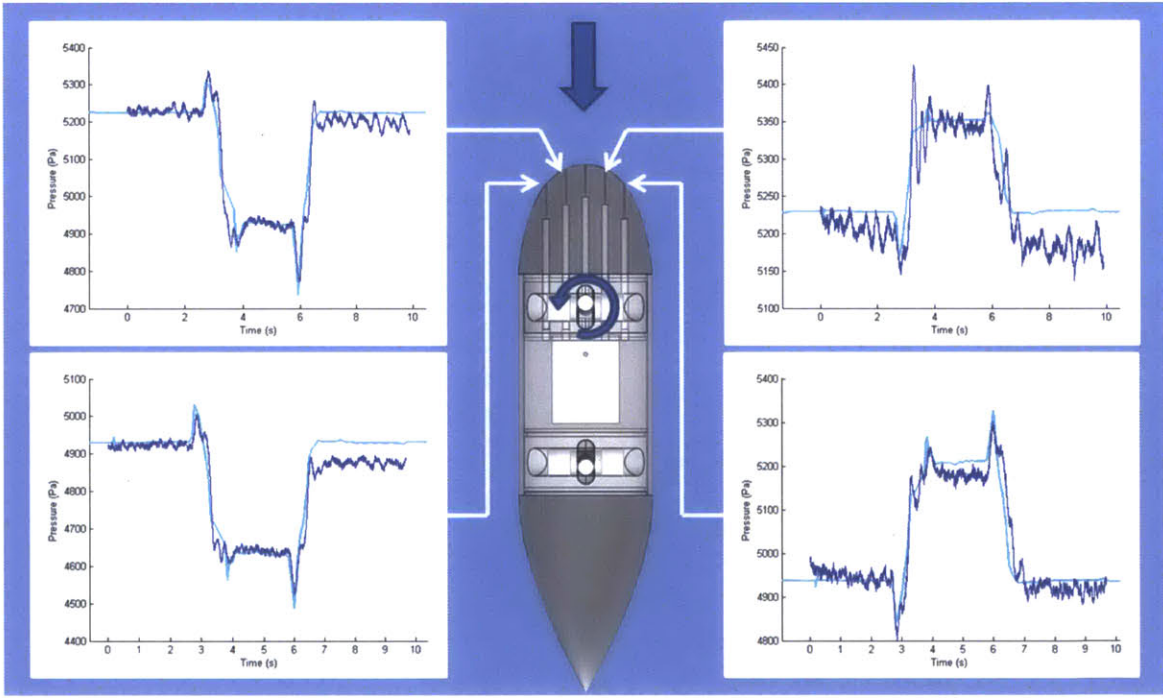


Figure A-3: Simulated (cyan) and experimentally measured (blue) pressure observed at 4 pressure sensors during a turn from 0 to 16 degrees and back to 0 degrees, with maximum acceleration of $65 \text{ deg}/s^2$. Pressure (Pa) is plotted against time (s). The blue arrow represents the direction of oncoming flow.

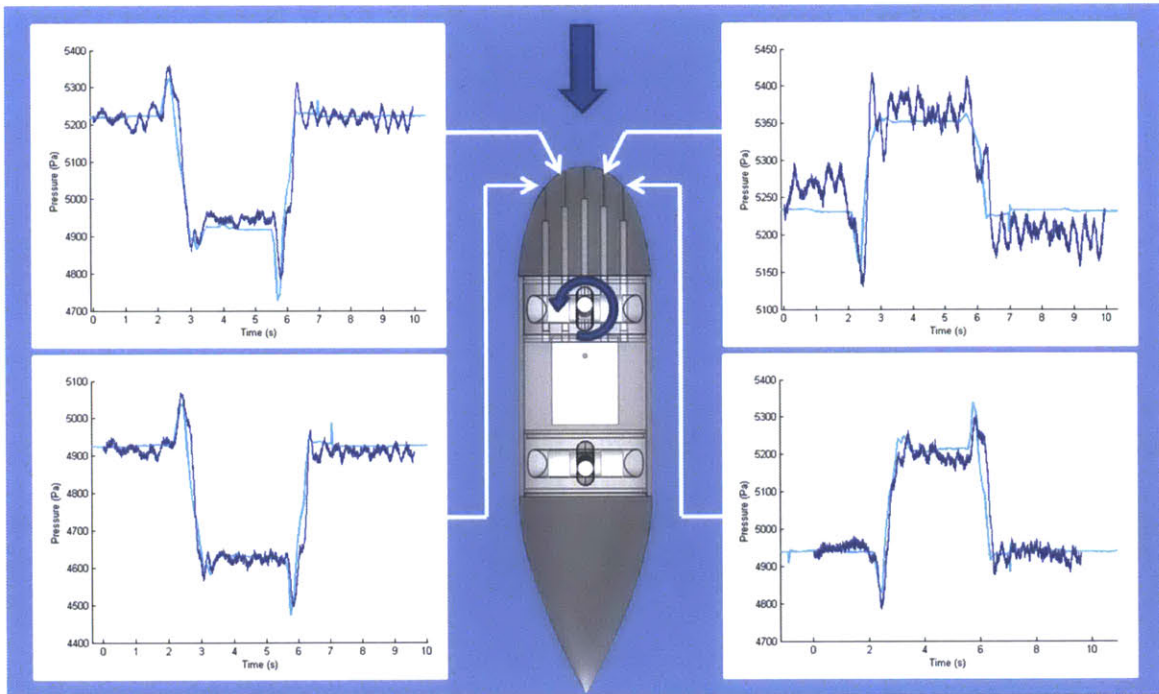


Figure A-4: Simulated (cyan) and experimentally measured (blue) pressure observed at 4 pressure sensors during a turn from 0 to 16 degrees and back to 0 degrees, with maximum acceleration of 100 deg/s^2 . Pressure (Pa) is plotted against time (s). The blue arrow represents the direction of oncoming flow.

Appendix B

Results from Various UKF Parameter Settings

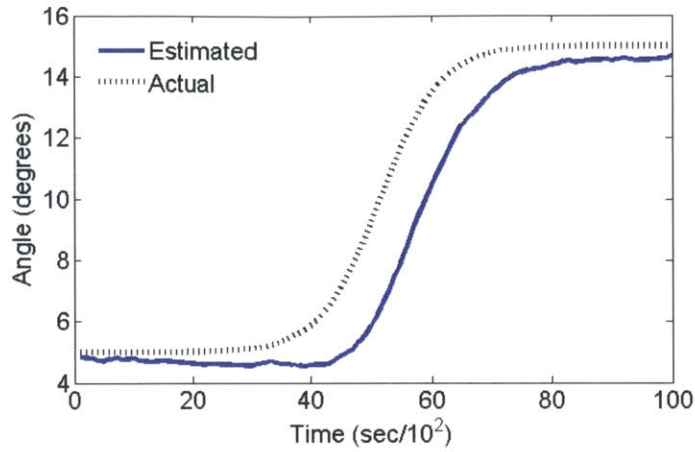


Figure B-1: Setting the measurement noise covariance to 10x the actual measurement noise reduces estimate oscillation, but increases the time delay, as shown in this simulation.

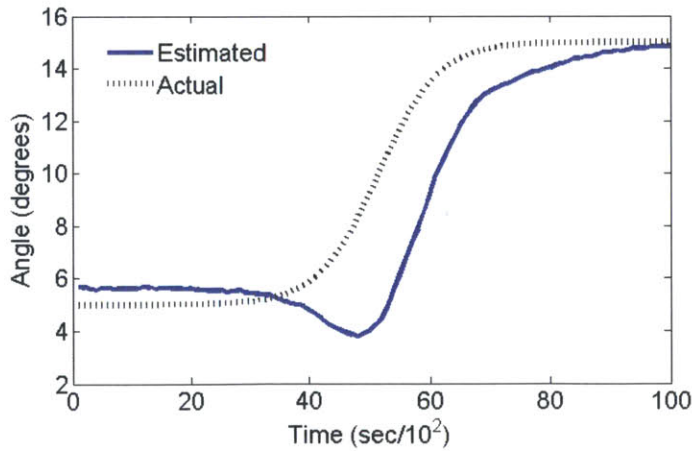


Figure B-2: Setting the process noise covariance of yaw rate to 1/10th the noise covariance in yaw angle is shown to cause undershoot behavior which follows that in the measurement. This indicates some relationship between allowable unmodeled state change and estimated process noise.

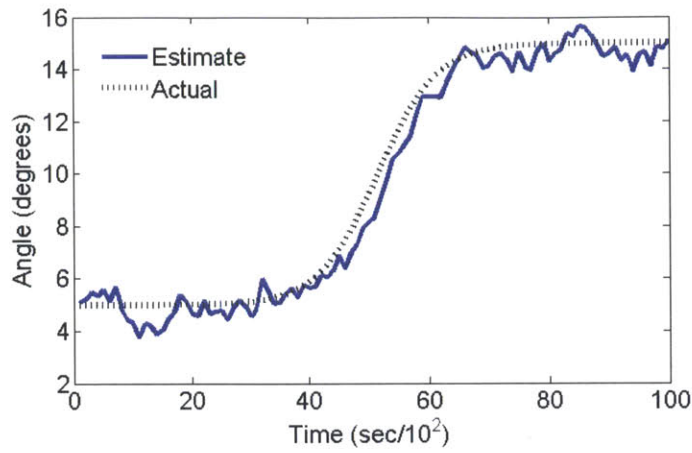


Figure B-3: UKF angle estimation produced by a simulated system with 4 sensors.

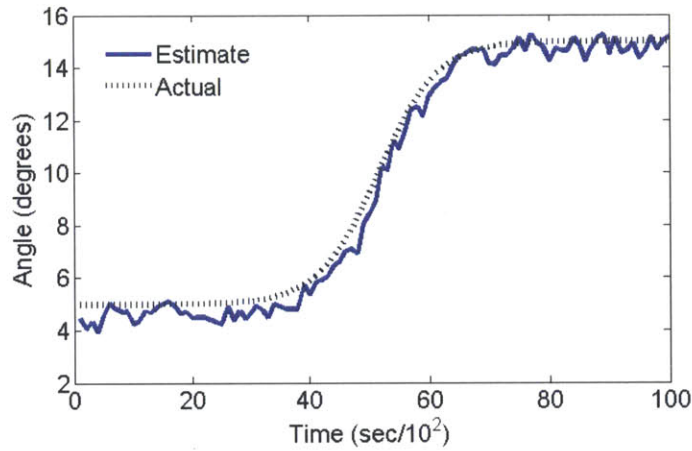


Figure B-4: UKF angle estimation produced by a simulated system with 8 sensors.

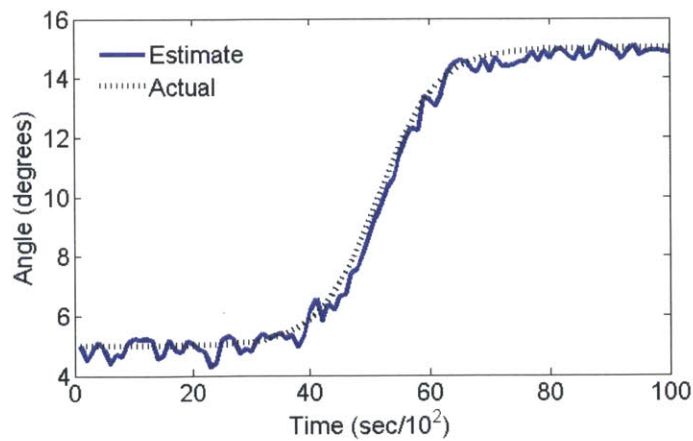


Figure B-5: UKF angle estimation produced by a simulated system with 18 sensors.

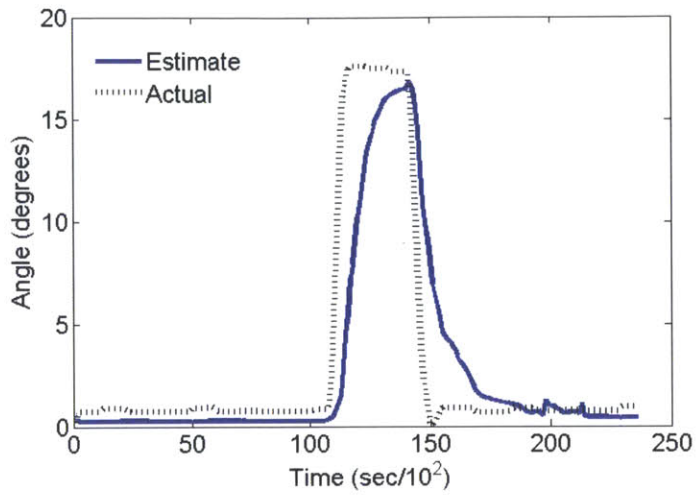


Figure B-6: An experimental profile was provided to a simulated system capable of outputting model-accurate pressure measurements. The result demonstrates the dependence of convergence rate on the estimated measurement noise covariance (here, $R=70$).

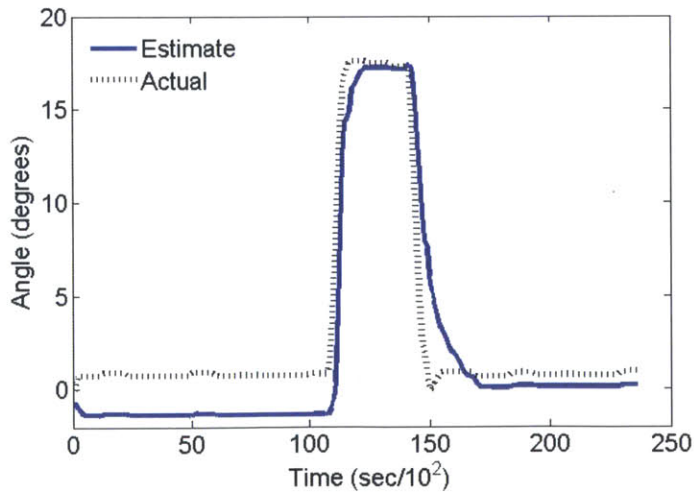


Figure B-7: Simulation with an estimated measurement noise covariance of $R=20$.

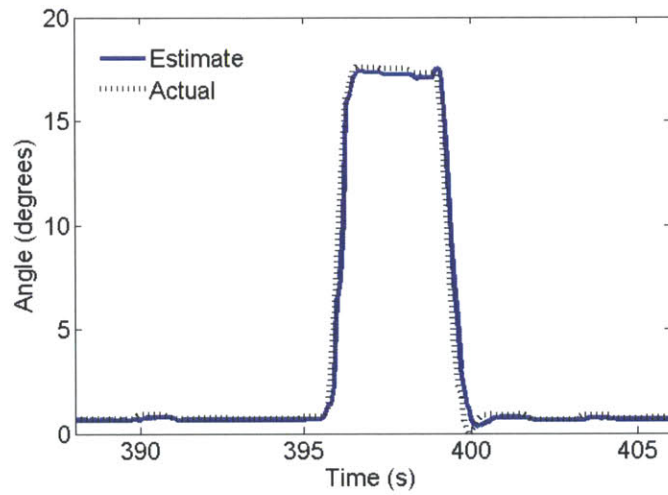


Figure B-8: Simulation with an estimated measurement noise covariance of $R=3$. This case demonstrates the accuracy of the UKF state estimate when the measurement noise in the system is negligible. However, for the cases applied to experimental data, the high measurement noise introduces more oscillation of the estimate.

Bibliography

- [1] J M Anderson and P A Kerrebrock. The vorticity control unmanned undersea vehicle - An autonomous vehicle employing fish swimming propulsion and maneuvering. *Tenth International Symposium on Unmanned Untethered Submersible Technology*, pages 189–195, 1997.
- [2] C F Baker and J C Montgomery. Lateral line mediated rheotaxis in the Antarctic fish *Pagothenia borchgrevinki*. *Polar Biology*, 21:305–309, 1999.
- [3] H Bleckman and G Topp. Surface wave sensitivity of the lateral line organs of the topminnow *Aplocheilus lineatus*. *Naturwissenschaften*, 68:624–625, 1981.
- [4] V Braitenberg. *Vehicles: Experiments in synthetic psychology*. The MIT Press, 1984.
- [5] T Burt de Perera. Fish can encode order in their spatial map. *Proceedings of the Royal Society*, 271:2131–2134, 2004.
- [6] J Chen, J Engel, N Chen, S Pandya, S Coombs, and C Liu. Artificial lateral line and hydrodynamic object tracking. pages 694–697, Istanbul, 2006. 19th IEEE Conference on Micro Electrical Mechanical Systems.
- [7] J E Colgate and K M Lynch. Control problems solved by a fish’s body and brain: a review. *IEEE Journal of Oceanic Engineering*, 39(3):660–673, 2004.
- [8] J Conte, Y Modarres-Sadeghi, M N Watts, F S Hover, and M S Triantafyllou. A fast-starting mechanical fish that accelerates at 40 m s^{-2} . *Bioinspir. Biomim.*, page 035004, 2010.
- [9] S Coombs. Signal detection theory, lateral-line excitation patterns and prey capture behaviour of mottled sculpin. *Animal Behavior*, 58:421–430, 1999.
- [10] S Coombs, C Braun, and B Donovan. The orienting response of Lake Michigan mottled sculpin is mediated by canal neuromasts. *The Journal of Experimental Biology*, 204:337–348, 2001.
- [11] S Coombs, P Görner, and H Münz. *The Mechanosensory Lateral Line: Neurobiology and Evolution*. Springer, 1989.

- [12] S Coombs, M Hastings, and J Finneran. Modeling and measuring lateral line excitation patterns to changing dipole source locations. *Journal of Comparative Physiology A*, 178:359–371, 1996.
- [13] E J Denton and J Gray. Mechanical factors in the excitation of clupeid lateral lines. *Proceedings of the Royal Society of London B*, 218(1210):1–26, 1983.
- [14] E J Denton and J Gray. *Sensory Biology of Aquatic Animals*. Springer-Verlag, 1988.
- [15] Z Fan, J Chen, J Zou, J Li, C Liu, and F Delcomyn. Development of artificial lateral-line flow sensors. *Solid-State Sensor, Actuator and Microsystems Workshop*, 2002.
- [16] V Fernandez, A Maertens, F Yaul, J Dahl, J Lang, and M S Triantafyllou. Lateral-line-inspired sensor arrays for navigation and object identification. *Marine Technology Society Journal*, 2011.
- [17] J P Fransch, H J A Hagedorn, J Goulet, J Engelmann, and J L van Hemmen. Wake Tracking and the Detection of Vortex Rings by the Canal Lateral Line of Fish. *Physical Review Letters*, 103:078102, 2009.
- [18] J Goulet, J Engelmann, B P Chagnaud, J P Fransch, M D Suttner, and J L van Hemmen. Object localization through the lateral line system of fish: theory and experiment. *Comparative Physiology A*, 194:1–17, 2008.
- [19] B Harris. *The Navy Times book of submarines: A political, social, and military history*. Berkley, 1989.
- [20] E S Hassan. On the discrimination of spatial intervals by the blind cave fish. *Journal of Comparative Physiology A*, 159:701–710, 1986.
- [21] J L Hess and A M O Smith. Calculation of nonlifting potential flow about arbitrary three-dimensional bodies. *J. Ship Res.*, 8:22–44, 1964.
- [22] D Hoekstra and J Janssen. Non-visual feeding behavior of the mottled sculpin, *Cottus bairdi*, in Lake Michigan. *Environ. Biol. Fishes*, 12:111–117, 2006.
- [23] S F Hoerner. *Fluid-dynamic drag*. Hoerner Fluid Dynamics, 1965.
- [24] T Hsieh, S Huang, L Mu, E Chen, and J Guo. Artificial lateral line design for robotic fish. *2011 IEEE Symposium on Underwater Technology and Workshop on Scientific Use of Submarine Cables and Related Technologies*, pages 1–6, April 2011.
- [25] H Hu. Biologically inspired design of autonomous robotic fish at Essex. *IEEE SMC UK-RI Chapter Conference, on Advances in Cybernetic Systems*, page 38, 2006.

- [26] S J Julier and J K Uhlmann. Unscented filtering and nonlinear estimation. *Proceedings of the IEEE*, 92(3):401–422, 2004.
- [27] J Katz and A Plotkin. *Low Speed Aerodynamics*. Cambridge University Press, 2001.
- [28] A G P Kottapalli, C W Tan, M Olfatnia, J M Miao, G Barbastathis, and M S Triantafyllou. Liquid crystal polymer membrane MEMS sensor for flow rate and flow direction sensing applications. *Journal of Micromechanics and Microengineering*, 21, 2011.
- [29] J C Liao. The role of the lateral line and vision on body kinematics and hydrodynamic preference of rainbow trout in turbulent flow. *The Journal of Experimental Biology*, 209:4077–4090, 2006.
- [30] A Maertens. Touch at a distance: Underwater object identification using pressure sensors. Master’s project, Massachusetts Institute of Technology, 2009.
- [31] M E McConney, N Chen, D Lu, H A Hu, S Coombs, C Liu, and V V Tsukruk. Biologically inspired design of hydrogel-capped hair sensors for enhanced underwater flow detection. *Soft Matter*, 5(2):292–295, 2008.
- [32] M J McHenry, K E Feitl, J A Strother, and W J Van Trump. Larval zebrafish rapidly sense the water flow of a predator’s strike. *Biology Letters*, 5(4):477–479, 2009.
- [33] J Mogdans and H Bleckmann. Responses of the goldfish trunk lateral line to moving objects. *Journal of Comparative Physiology*, 182:659–676, 1998.
- [34] J C Montgomery, C F Baker, and A G Carton. The lateral line can mediate rheotaxis in fish. *Nature*, 389:960–963, 1997.
- [35] John C Montgomery, Sheryl Coombs, and Cindy F Baker. The mechanosensory lateral line system of the hypogean form of *Astyanax fasciatus*. pages 87–96, 2001.
- [36] J N Newman. *Marine Hydrodynamics*. The MIT Press, 1977.
- [37] S Pandya, Y Yang, D L Jones, J Engel, and C Liu. Multisensor Processing Algorithms for Underwater Dipole Localization and Tracking Using MEMS Artificial Lateral-Line Sensors. *EURASIP Journal on Applied Signal Processing*, 2006:1–8, 2006.
- [38] B L Partridge and T J Pitcher. The sensory basis of fish schools: relative roles of lateral line and vision. *Comp. Physiol. A*, 135:315–325, 1980.
- [39] S Peleshanko, M D Julian, M Ornatska, M E McConney, M C LeMieux, N Chen, C Tucker, Y Yang, C Liu, J A Humphrey, and V V Tsukruk. Hydrogel-Encapsulated Microfabricated Haircells Mimicking Fish Cupula Neuromast. *Advanced Materials*, 19(19):2903–2909, 2007.

- [40] M Plath, J Parzefall, K E Körner, and I Schlupp. Sexual selection in darkness? Female mating preferences in surface- and cave-dwelling Atlantic mollies, *Poecilia mexicana*(Poeciliidae, Teleostei). *Behav Ecol Sociobiol*, 55:596–601, 2004.
- [41] M A B Schwalbe, D K Bassett, and J F Webb. Feeding in the dark: lateral-line-mediated prey detection in the peacock cichlid *Aulonocara stuartgranti*. *The Journal of experimental biology*, 215:2060–71, June 2012.
- [42] R Venturelli, O Akanyeti, F Visentin, J Jezov, L D Chambers, G Toming, J Brown, M Kruusmaa, W M Megill, and P Fiorini. Hydrodynamic pressure sensing with an artificial lateral line in steady and unsteady flows. *Bioinspir. Biomim.*, 7:036004, 2012.
- [43] G D Weymouth and D K P Yue. Physics-Based Learning Models for Ship Hydrodynamics. *Journal of Ship Research*, in review, 2012.
- [44] T T Whitfield. Lateral line: precocious phenotypes and planar polarity. *Current Biology*, 15(2):67–70, 2005.
- [45] S P Windsor and M J McHenry. The influence of viscous hydrodynamics on the fish lateral-line system. *Integr. Comp. Biol.*, 49(6):691–701, 2009.
- [46] S P Windsor, S E Norris, S M Cameron, G D Mallinson, and J C Montgomery. The flow fields involved in hydrodynamic imaging by blind Mexican cave fish (*Astyanax fasciatus*). *The Journal of experimental biology*, 213:3832–42, 2010.
- [47] Y Yang, N Nguyen, N Chen, M Lockwood, C Tucker, H Hu, B Horst, C Liu, and D L Jones. Artificial lateral line with biomimetic neuromasts to emulate fish sensing. *Bioinspiration & biomimetics*, 5(1):16001, 2010.
- [48] F Yaul. A flexible underwater pressure sensor array for artificial lateral line applications. Master’s project, Massachusetts Institute of Technology, 2011.